Microphysical aerosol properties retrieved from combined lidar and sun photometer measurements

MASTER THESIS

submitted to
the Faculty of Physics and Earth Sciences
of Leipzig University

to award the academic degree
Master of Science

handed in on 6 January 2012 by
B. Sc. Janet Wagner

Supervisor: Dr. Ulla Wandinger

Reviewer: PD Dr. Albert Ansmann
Prof. Dr. Manfred Wendisch

Contents

Chapter 1

Introduction

Meteorology deals with atmospheric phenomena which are based on physical and chemical laws. They are often caused by solid or liquid particles which float through the surrounding air. These particles are called aerosol particles. They affect, e.g., the formation of clouds and interact with solar radiation. They also influence the human health, and they can have an impact on the ozone depletion or acid rain. Especially the influence of aerosol particles on the local weather and the global climate makes it important to determine the type and constitution of atmospheric aerosols.

There are several methods for the observation and measurement of aerosol particles to assess information about their optical, microphysical, and radiative properties. At the Leibniz Institute for Tropospheric Research Leipzig (IfT Leipzig) a lidar and a sun photometer are in use for the remote sensing of aerosol properties. Lidar is the short form of **Li**ght **D**etection **a**nd **R**anging. It is an active remote-sensing method that allows measurements with high temporal and spatial resolution. Regular measurements at IfT Leipzig are carried out with MARTHA, the **M**ultiwavelength **A**tmospheric **R**aman Lidar for **T**emperature, **H**umidity and **A**erosol profiling, within the **E**uropean **A**erosol **R**esearch **LI**dar **NET**work (EARLINET, *EARLINET-Homepage* (2011)). In addition, a sun photometer provides spectrally resolved information about aerosols for the whole vertical column. These measurements are part of the **AE**rosol **RO**botic **NET**work (AERONET) which operates worldwide (*AERONET-Homepage*, 2011a).

Results of the lidar measurements are height profiles of the backscatter and the extinction coefficient at two or three different wavelengths. From backscattering and extinction information about the aerosol type can be obtained through the calculation of the lidar ratio and the Ångström exponent. Microphysical properties are usually retrieved by use of a rigorous mathematical approach (*Ansmann and Müller*, 2005). The mentioned parameters can be specified for certain heights. For example, a separation of boundary-layer aerosol and free-tropospheric aerosol is possible.

Depending on the detecting telescope of the lidar, there is always a height range in the lower atmosphere that is not covered. This deficiency is caused by the overlap effect and is due to the optical and geometrical setup of the lidar system (*Wandinger*, 2005). For a far-range telescope the layer influenced by the overlap effect reaches from the ground up to several kilometres. A near-range telescope could provide trustworthy data down to 100 m, but it has a lag of information in the higher atmosphere above 2–5 km. The overlap effect can partly be corrected by determination of the lidar overlap profile (*Wandinger and Ansmann*, 2002).

Sun photometer measurements refer to the whole range of the atmosphere from the ground to the stratosphere. The instruments detect the direct sun radiance as well as the diffuse sky radiance at several wavelengths. Besides optical properties, such as the aerosol optical thickness and the Ångström exponent, also microphysical as well as radiative properties can be retrieved by use of inversion algorithms (*Dubovik and King*, 2000; *O'Neill et al.*, 2003). Radiometric measurements give information about the amount of the aerosol and further a more detailed characterization of the aerosol type than through lidar measurements, for example the separation in different modes.

Sun photometer measurements can only be carried out during clear-sky conditions and at daytime (*Holben et al.*, 1998). Unfortunately, there is no information available to which specific height range the retrieved parameters refer. By use of height-resolved profiles of the aerosol particle concentration, which show where the aerosol is located, the assignment of the properties to a certain layer and a better classification would be possible. Therefore, the combination of the radiometric information with the lidar profiles seems to be very prospective.

Usually it is rather difficult to classify aerosols. At IfT Leipzig different aerosol types can be observed, which have sources not only within Europe, but also on other continents. Aerosol particles in the planetary boundary layer often originate from local and regional emissions (*Wandinger et al.*, 2004). Most important are polluted aerosols from industrial regions in Central, East, or Southeast Europe. Free-tropospheric aerosol particles are advected through long-range transport. The intercontinental carriage allows the observation of aerosol which originates from forest fires in North America or Siberia as well as of Saharan dust or Arctic haze (*Mattis et al.*, 2008).

Especially for aerosol mixtures which consist of different types of particles, a separation in different size modes can be useful. In accordance to the size distribution obtained from radiometric measurements, in this work aerosol particles are separated in fine-mode and coarse-mode particles (*AERONET-Homepage*, 2011b). The fine mode is determined by particles with a radius smaller than 0.5 μm, whereas the coarse mode consists of particles with a radius bigger than 0.5 μm. Contribution to the fine mode is usually due to smoke and combustion aerosols as well as industrial aerosols. Dust and ash cause mainly coarse-mode events. The different aerosol types can be characterized through optical properties, such as the Ångström exponent, the lidar ratio, and the depolarization ratio. Values can be found, e.g., in *Müller et al.* (2005, 2007) and *Wandinger et al.* (2002, 2010).

Combined data of both lidar and sun photometer would provide an almost complete image of the atmosphere. It seems to be a promising approach for the atmospheric aerosol research. Older studies already dealt with combined lidar and radiometric measurements, e.g., to obtain a depth-integrated complex refractive index (*Spinhirne et al.*, 1980). Another approach referred to height profiles of the particle size distribution (*Reagan et al.*, 1977), but did not show good agreement with simultaneous aircraft measurements. Both instruments have to measure at the same time and location in order to guarantee the observation of the same ensemble of aerosol particles. Within the European project ACTRIS (**A**erosol, **C**louds and **T**race Gas **R**esearch **I**nfrastructure **N**etwork) such simultaneous measurements of lidar and sun photometer are realized (*ACTRIS-Homepage*, 2011). Since April 2011, IfT Leipzig coordinates the work package "Lidar and sun photometer" of ACTRIS. The main focus lies on the improvement of daytime observations of lidar instruments as well as on the development of combined inversion algorithms.

This work deals with a software package which was provided by *Chaikovsky et al.* (2008). Based on lidar measurements at the three wavelength 355, 532, and 1064 nm and radiometric data, such as aerosol optical thickness and volume concentration of different aerosol modes, a numerical algorithm was developed which combines these information. The results are altitude distributions of fine and coarse particles. In aerosol applications, mathematical inversion schemes are commonly used to retrieve microphysical and radiative properties. The underlying methods can be found, e.g., in the books by *Twomey* (1977) and *Tikhonov and Arsenin* (1977). The algorithm for the combination of lidar and sun photometer measurements is based on an optimal-estimation technique under use of all available measurements. Problematic is the observation at different wavelengths by lidar instruments and sun photometers. However, *Dubovik* *et al.* (2006) developed an inversion algorithm that calculates backscatter and extinction coefficients from sky radiance information for the corresponding lidar wavelengths. These coefficients are also used as input data for the retrieval algorithm.

The main task of this work was a test of the retrieval software in order to identify weaknesses and thus contribute to the further improvement of the inversion algorithm. Specific aerosol situations were chosen that were already broadly evaluated, so that an assessment of the results was possible. In particular, three cases are considered representing Saharan dust, smoke and industrial aerosol from East Europe, and volcanic aerosol from the Eyjafjallajökull eruption. Saharan dust consists mainly of coarse particles, whereas the observation case of aerosol from East Europe was a pure fine-mode event. In addition, the volcanic aerosol is a mixture of fine-mode and coarse-mode particles. This sample of case studies allows a test of the sensitivity of the retrieval algorithm to specific aerosol types.

Chapter 2 of this work gives an overview about the measurement systems and the retrieved aerosol properties. Thus lidar and sun photometer are described as well as the underlying theoretical background which includes the calculation of the mentioned parameters. In Chapter 3, the retrieval algorithm is examined in detail. The chapter covers the overlap correction of the lidar data as well as the assimilation of radiometric measurements to the lidar data. The derivation of a set of equations, which is the basis of the numerical algorithm, is explained. The concept of the data preparation and evaluation is presented in Chapter 4. Tools for the assessment of the meteorological situation and the identification of aerosol sources are introduced. Chapter 5 presents the case studies. Based on the cases of 6 April 2009 and 30 May 2008 some crucial issues of the retrieval algorithm are demonstrated and the errors are quantified. Furthermore, on the basis of measurements after the Eyjafjallajökull eruption on 14 April 2010 an application is suggested to distinguish between ash and non-ash particles in the ash plume. The approach makes use of the separation of fine-mode and coarse-mode backscatter coefficients. The results are compared with findings from a method that separates the backscatter coefficients based on depolarization measurements. Finally, Chapter 6 summarizes the results and gives suggestions for further improvements of the retrieval algorithm for combined lidar and sun photometer data.

Chapter 2

Measurement systems and retrieved aerosol properties

This work mainly examines the results from a retrieval of aerosol microphysical properties obtained from combined sun photometer and lidar data. This chapter covers the design of the measurement instruments and explains how optical and microphysical properties of aerosols can be retrieved. The data used as input for the retrieval algorithm are measured with a sun photometer and a multi-wavelength Raman lidar. Both instruments are located at IfT Leipzig and are part of the international network AERONET and the European network EARLINET, respectively.

2.1 AERONET and EARLINET

AERONET consists of about 250 sun photometers which are permanently in use and are distributed worldwide. Nine of them are placed in Germany. Sun photometers can measure both direct sun radiance and diffuse sky radiance. Therefore, measurements are only carried out at daytime. The procedure allows the retrieval of aerosol optical, microphysical, and radiative properties (*Holben et al.*, 1998). Due to the worldwide distribution of the stations the investigation of different types of aerosols under varying conditions is possible. Information is not only gained locally but also on a regional and global scale. The measurement system is explained in Section 2.2. Retrieved properties are optical parameters such as the aerosol optical thickness (AOT) and the Ångström exponent (see Section 2.2.2) as well as microphysical parameters such as the aerosol size distribution (see Section 2.2.3).

The lidar network EARLINET consists of 31 stations (see Fig. 2.1). They are operated by scientific facilities on a voluntary basis to gain an aerosol climatology for Europe (*EARLINET-Homepage*, 2011). IfT Leipzig has been part of EARLINET since 2000. At every station three measurement sessions are carried out per week. Additional measurements take place for certain events like volcano eruptions, Saharan dust intrusions, or during the overflight of the CALIPSO satellite. The advantage of lidar observations is the high temporal and spatial resolution. That is why they are well suited for the observation of strongly variable parameters such as temperature, humidity, wind, aerosols, clouds, and trace gases (*Wandinger*, 2005). Section 2.3 describes the measurement system in more detail and also covers the retrieval of backscatter and extinction profiles.

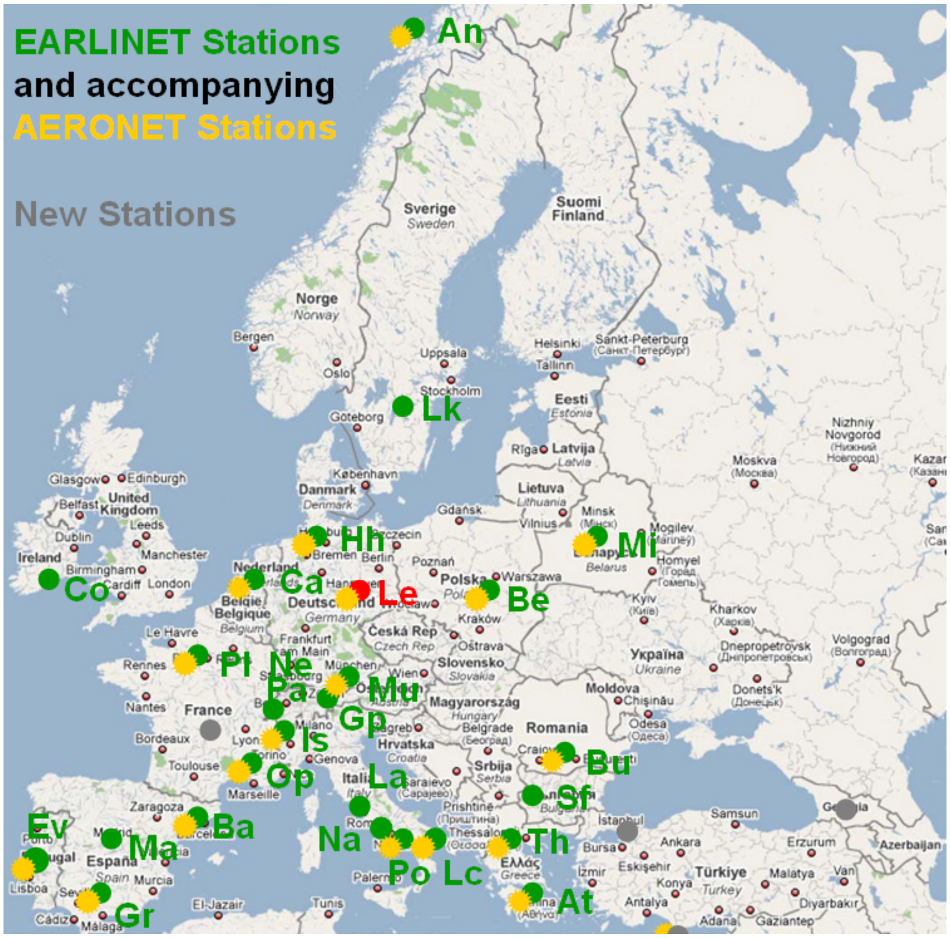

Figure 2.1: Overview of the distribution of the EARLINET stations (green) and the accompanying AERONET stations (yellow). Grey stations mark new stations. The location of IfT Leipzig is indicated in red. The station short names follow the EARLINET convention (*EARLINET-Homepage*, 2011).

2.2 Sun photometer

2.2.1 Instrument and data classification

Sun photometers applied by AERONET consist of a collimator, several interference filters, and two detectors for the measurement of direct sun, aureole, and sky radiance. They are all of the same type, produced by the company "CIMEL Electronique". At IfT Leipzig direct sun radiation is measured in eight bands (340, 380, 440, 500, 675, 870, 1020, 1640 nm), while sky radiation is obtained in four bands (440, 675, 870, 1020 nm). The incoming radiation is attenuated by atmospheric components. The attenuation is proportional to the amount of aerosol particles. Sky radiance observations are used for inversion algorithms to retrieve microphysical aerosol properties. It is necessary to perform the measurements under varying azimuth and elevation angles in order to get a wide range of scattering angles.

The atmosphere has to be free of clouds in order to get usable results, otherwise data have to be removed. A cloud-screening algorithm is carried out to proof the data. It is based on the variability of the optical thickness. Strong variations within a short time period indicate rather clouds than aerosols. Further information can be found in *Smirnov et al.* (2000). After cloud screening the data are classified as Level 1.5 data, while before they are Level 1.0 data. Another manual inspection is done during the calibration of the instruments. Level 2.0 data are available after the calibration which is done once per year. Level 1.0 and Level 1.5 data can be found on the AERONET website immediately.

2.2.2 Optical properties

Most important for characterizing aerosols are the AOT and the Ångström exponent. Both can be retrieved from direct sun measurements. The AOT is the optical depth caused by aerosol particles and can be understood as a measure of transmission through the atmosphere. The derivation of the AOT dependent on wavelength λ is based on the Lambert-Beer-Bouguer law which is used in the following form (*Holben et al.*, 1998):

$$U(\lambda) = U_0(\lambda) d^2 e^{-\tau(\lambda) m} T_y, \tag{2.1}$$

with

U – digital voltage,

U_0– calibration constant,
d – distance between earth and sun,
τ – optical thickness,
m – optical air mass,
T_y– transmission of absorbing gases.

The optical air mass m can be derived from the zenith angle Θ:

$$m = \frac{1}{\cos \Theta}. \tag{2.2}$$

It is the ratio between the actual and the shortest way of radiation through the atmosphere. The optical thickness τ in Eq. (2.1) contains contributions from both aerosols and air molecules. The latter is caused by Rayleigh scattering. Thus to get the AOT caused by aerosol extinction τ_{aer}, the influence of the molecules τ_{mol} has to be removed:

$$\tau_{aer}(\lambda) = \tau(\lambda) - \tau_{mol}(\lambda). \tag{2.3}$$

Usually, the AOT is calculated on the basis of both scattering and absorption, thus it is derived as the sum of the scattering optical thickness τ_{sca} and the absorption optical thickness τ_{abs}:

$$\tau_{aer} = \tau_{sca} + \tau_{abs}. \tag{2.4}$$

An empirical expression for the wavelength dependence of the optical thickness was found by Ångström in 1929 (*Ångström*, 1929):

$$\tau = t\lambda^{-\mathring{a}}, \tag{2.5}$$

where $\mathring{a}$ is the Ångström exponent and t the turbidity coefficient which equals τ for $\lambda = 1$ μm. For two different wavelengths a spectral expression for $\mathring{a}$ can be derived where t has cancelled out (*O'Neill et al.*, 2001):

$$\mathring{a} = -\frac{\mathrm{d} \ln \tau}{\mathrm{d} \ln \lambda} = -\frac{\ln\left[\tau(\lambda_1)/\tau(\lambda_2)\right]}{\ln\left[\lambda_1/\lambda_2\right]}. \tag{2.6}$$

The Ångström exponent is a useful indicator for the size of the aerosol particles. It increases with decreasing size and vice versa as the differences in the AOT for different wavelengths are larger for finer particles than for coarser particles.

2.2.3 Microphysical properties

From sky radiance measurements it is possible to gain microphysical aerosol properties such as the volume particle size distribution and its characteristics. An inversion algorithm is applied which was developed by *Dubovik and King* (2000). Further information about the development of the algorithm and a more detailed description are provided in the papers by *Dubovik et al.* (2000, 2002a,b, 2006) and *Sinyuk et al.* (2007). For this work, one should be aware of some assumptions on which the inversion retrieval is based.

First of all, it is assumed that the aerosol ensemble consists of spherical and non-spherical components. Both can be modeled by certain approaches. An ensemble of polydisperse, homogeneous spheres is used for the spherical part. The non-spherical part is modeled by a mixture of polydisperse, randomly-oriented homogeneous spheroids (*AERONET-Homepage*, 2011b). Furthermore, a fixed spheroid aspect ratio distribution is used and adjusted to the scattering matrix of mineral dust. The complex refractive index of the spheres and spheroids is the same for all particle sizes. Further assumptions are the vertically homogeneous distribution of the aerosol in a plane-parallel atmosphere and the surface reflectance which is approximated by a bidirectional reflectance distribution function.

The retrieved volume particle size distribution covers the range of radii from 0.05 up to 15 μm in 22 logarithmically equidistant bins. Also, the percentage of spherical particles as well as the real and imaginary parts of the complex refractive index are provided, the latter ones for the different measurement wavelengths. The size distribution can be separated in fine-mode and coarse-mode particles. This is done by finding the minimum of the bimodal distribution between 0.439 and 0.992 μm. With the inversion algorithm all microphysical properties as well as the optical thickness are calculated not only for the total content of aerosol but also for fine-mode and coarse-mode particles separately. Besides the mentioned complex refractive index, the effective radius, the volume mean radius, the standard deviation, and the volume concentrations are given.

The volume concentration V_c of the aerosol column in $\mu\text{m}^3/\mu\text{m}^2$ is calculated as follows (*AERONET-Homepage*, 2011b):

$$V_c = \int\limits_{r_{min}}^{r_{max}} \frac{\mathrm{d}V(r)}{\mathrm{d}\ln r} \mathrm{d}\ln r, \tag{2.7}$$

where $\frac{\mathrm{d}V(r)}{\mathrm{d}\ln r}$ is the volume size distribution on a logarithmic scale. As the size range of the particles covers several orders of magnitude, it is convenient to use a logarithmic presentation of the distribution. On a linear scale only one peak would appear, while on a logarithmic scale the fine and coarse modes are well manifested. Furthermore, the size distribution shows up as a normal distribution in the logarithmic diagram. Thus, as the log-normal distribution is characterized by the geometric mean radius and standard deviation, another advantage of this presentation is the direct derivation of aerosol particle properties. For spheres the volume size distribution can be expressed in terms of the particle number concentration $N(r)$ as follows:

$$\frac{dV(r)}{\mathrm{d}\ln r} = V(r)\frac{\mathrm{d}N(r)}{\mathrm{d}\ln r} = \frac{4}{3}\pi r^3 \frac{\mathrm{d}N(r)}{\mathrm{d}\ln r}. \tag{2.8}$$

2.2.4 Radiative properties

Besides optical and microphysical properties also radiative properties can be derived. They are calculated on the basis of microphysical parameters retrieved with the AERONET inversion algorithm. Most important are the single-scattering albedo ω and the real scattering matrix $\mathbf{F}(\theta, \phi)$ dependent on the scattering angle θ and the azimuth angle ϕ. ω dependent on λ is given by the following ratio:

$$\omega(\lambda) = \frac{\tau_{sca}}{\tau_{aer}}. \tag{2.9}$$

It describes how much of the radiation is scattered or absorbed ($\omega = 0$ means no scattering and $\omega = 1$ no absorption).

The scattering matrix describes the scattering properties of particles. It contains all the information about the transformation from incident light into scattered light. The assumption of randomly-oriented and symmetric particles leads to a simplified form of the scattering matrix, the so called Lorenz-Mie structure, that is used in the retrieval algorithm:

$$\mathbf{F}(\Theta) = \begin{pmatrix} F_{11}(\Theta) & F_{12}(\Theta) & 0 & 0 \\ F_{12}(\Theta) & F_{22}(\Theta) & 0 & 0 \\ 0 & 0 & F_{33}(\Theta) & F_{34}(\Theta) \\ 0 & 0 & -F_{34}(\Theta) & F_{44}(\Theta) \end{pmatrix}.$$

Even though radiometric measurements allow a broad characterization of the aerosols, there is no information about the height where the aerosol particles are located. It is assumed that most of them (80%–95%) are located in the planetary boundary layer and therefore, the retrieved properties belong to the lowest 1 to 2 km of the troposphere.

However, that is not true for all situations and it is one of the reasons why additional lidar measurements are so valuable.

2.3 Raman lidar

2.3.1 Instrumental setups

At IfT Leipzig the multiwavelength Raman lidar MARTHA is used for regular aerosol observations. Fig. 2.2 shows the principle construction of MARTHA with its transmitter and receiver units. Within the transmitter unit a Nd:YAG laser emits infrared light at 1064 nm. Frequency doubling and tripling is used to produce light at 532 and 355 nm, respectively. To reduce the divergence of the laser beam, the beam is expanded and emitted afterwards. The backscattered light is detected with a short-range telescope with a diameter of 20 cm and a far-range telescope with a diameter of 80 cm at the same time. The short-range telescope has a larger field of view of 4.1 mrad than the far-range one with only 0.5 mrad. The field of view is understood as the volume from which light reaches the receiving optics. The smaller the field of view the higher the maximum height from which backscattered light is received because of a better signal-to-noise ratio. However, a larger field of view allows the measurement in a shorter distance from the lidar. The backscattered light is directed to the beam-separation unit where it can be detected in dependence on wavelength and polarization state. A computer acquires the signals after they were transformed from optical to electronic ones.

The beam-separation unit of the far-range telescope has 10 channels. It discriminates the elastically backscattered light at the three outgoing wavelengths 355, 532, and 1064 nm which are used for the determination of the backscatter profiles. In addition, the Raman signals of nitrogen at 387 and 607 as well as of water vapor at 407 nm can be detected. This allows the derivation of the extinction profiles as well as of profiles of the lidar ratio at 355 and 532 nm. Two more channels refer to the pure rotational Raman signals of nitrogen at 532 nm. Furthermore, the 532-nm backscatter signal can be separated in a cross-polarized and a parallel-polarized component by use of a polarizer. Thus depolarization ratios can be derived. Further quantities which can be measured are the water-vapor mixing ratio and the temperature.

Since 22 September 2011 also reliable data are available from the near-range telescope. The 5-channel receiver detects the three elastic-backscatter signals at 355, 532, and

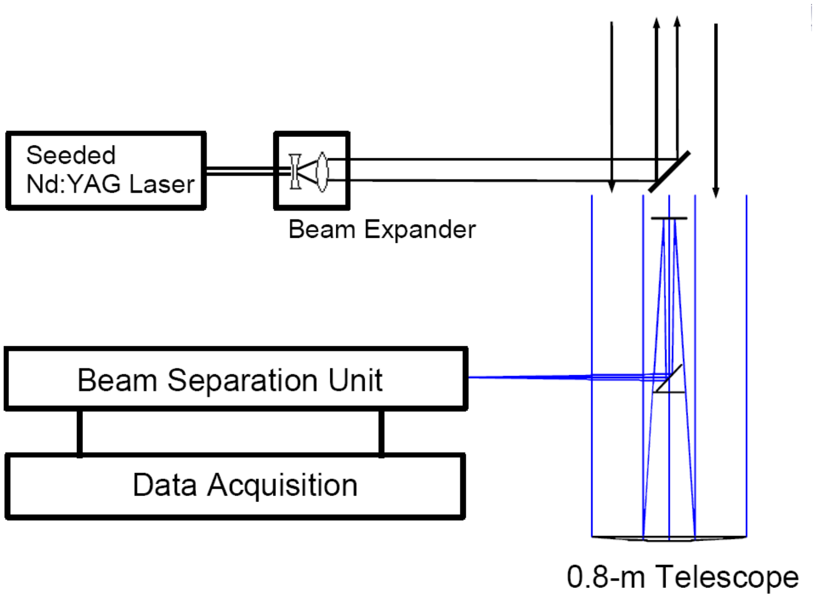

Figure 2.2: Principle construction of the Raman lidar MARTHA. The transmitter consists of a seeded Nd:YAG laser with a beam expander. The backscattered light is detected with a 0.8-m telescope and 0.2-m telescope (not shown). It is directed to the beam-separation unit and the data acquisition system.

1064 nm as well as the Raman-scattered signals of nitrogen at 387 and 607 nm. Thus the retrieved quantities are backscatter profiles at the three outgoing wavelengths, together with extinction profiles and lidar ratios at 355 and 532 nm, respectively.

2.3.2 Derivation of backscatter and extinction coefficients

The optical properties measured with a Raman lidar are backscatter and extinction coefficients β and α, respectively. They characterize interaction between radiation and aerosol particles (index aer) as well as molecules (index mol). Light can be scattered and absorbed. Scattering is described by the scattering coefficient α_{sca} and absorption by the absorption coefficient α_{abs}. The sum of both gives the extinction coefficient α dependent on height z and wavelength λ. It is as measure of the attenuation of the radiation intensity. The backscatter coefficient describes what part is scattered under 180° backwards to the lidar. Under consideration of all contributions, the following expressions for backscatter and extinction coefficients can be derived:

$$\alpha(\lambda, z) = \alpha_{aer,sca}(\lambda, z) + \alpha_{aer,abs}(\lambda, z) + \alpha_{mol,sca}(\lambda, z) + \alpha_{mol,abs}(\lambda, z), \tag{2.10}$$

$$\beta(\lambda, z) = \beta_{aer}(\lambda, z) + \beta_{mol}(\lambda, z). \tag{2.11}$$

Both measures are dependent on the number and the kind of particles and molecules.

It is also possible to obtain particle and molecular optical thicknesses from lidar measurements. They can be calculated from the extinction coefficients α_{aer} and α_{mol}:

$$\tau_{aer}(z) = \int_0^z \alpha_{aer}(\zeta)\mathrm{d}\zeta, \tag{2.12}$$

$$\tau_{mol}(z) = \int_0^z \alpha_{mol}(\zeta)\mathrm{d}\zeta. \tag{2.13}$$

The calculation of backscatter and extinction coefficients is based on the lidar equation. Its general form describes the received laser power P from a distance z in the following way (*Ansmann and Müller*, 2005):

$$P(z) = P_0 \frac{EO(z)}{z^2} \beta(z) \exp\left[-2\int_0^z \alpha(\zeta)\mathrm{d}\zeta\right], \tag{2.14}$$

where

$$z = \frac{ct}{2} \tag{2.15}$$

denotes the distance to the scattering object obtained from the velocity of light c and the time t needed between emitting the laser pulse and detecting the scattered light. Furthermore, it is

P_0 – emitted laser power,
E – system function,
$O(z)$ – overlap function.

The system function E describes the efficiency of the receiving optics and the detection system. The overlap function takes the geometric overlapping of the laser beam and the field of view of the receiving telescope into account. $O(z) = 1$ if the telescope maps the laser beam completely. The overlap effect leads to big uncertainties in the calculation of backscatter and extinction coefficients. As it is also a critical point in the retrieval algorithm, the effect and its correction is described in more detail in Section 2.3.3.

When Eq. (2.10) and (2.11) are taken into account, the lidar equation (2.14) becomes:

$$\begin{aligned} P(z) = P_0 \frac{EO(z)}{z^2} (\beta_{aer}(\lambda, z) + \beta_{mol}(\lambda, z)) \\ \times \exp\left[-\int_0^z (\alpha_{aer,sca}(\lambda,\zeta) + \alpha_{aer,abs}(\lambda,\zeta) + \alpha_{mol,sca}(\lambda,\zeta) + \alpha_{mol,abs}(\lambda,\zeta))\mathrm{d}\zeta\right]. \end{aligned} \tag{2.16}$$

While molecular backscattering and extinction can be calculated from meteorological data, particle backscatter and extinction coefficients are unknown values. To gain at least one coefficient from Eq. (2.16) the aerosol lidar ratio $S(\lambda, z)$, which describes the ratio between extinction and backscattering, is introduced:

$$S(\lambda, z) = \frac{\alpha_{aer}(\lambda, z)}{\beta_{aer}(\lambda, z)}. \tag{2.17}$$

For certain aerosols $S(\lambda, z)$ is fairly well known and the extinction coefficient in the lidar equation can be replaced. Thus the backscatter coefficient for the three wavelengths 355, 532, and 1064 nm can be calculated by applying the Klett-Fernald method (*Klett*, 1981; *Fernald*, 1984).

With the Raman lidar MARTHA it is also possible to receive inelastic or Raman-scattered signals. Raman scattering occurs when light is scattered by molecules. The light undergoes a wavelength shift when the scattering molecule experiences a transition to another vibration and/or rotation state, i.e., energy is exchanged between the scattered photon and the molecule. With MARTHA Raman scattering from nitrogen at 387 nm and from water vapor at 407 nm, for the emitting wavelength of 355 nm, and from nitrogen at 607 nm for 532 nm laser wavelength is detected.

The lidar equation for the inelastic Raman signal takes the following form:

$$\begin{aligned} P(z, \lambda_0, \lambda_R) = P_0 \frac{EO(z, \lambda_R)}{z^2} \beta_R(z, \lambda_o) \\ \times \exp\left[-\int_0^z [\alpha_{aer}(\lambda_0, \zeta) + \alpha_{aer}(\lambda_R, \zeta) + \alpha_{mol}(\lambda_0, \zeta) + \alpha_{mol}(\lambda_R, \zeta)] \mathrm{d}\zeta\right]. \end{aligned} \tag{2.18}$$

Light is scattered and attenuated at λ_0 on its way to the scattering object and at λ_R on its way back. Backscattering is only due to Raman scattering by molecules, and the corresponding backscatter coefficient $\beta_R(z, \lambda_0)$ is well known for molecules of known concentration such as nitrogen. Also, molecular extinction can be obtained from temperature and pressure profiles of the atmosphere. Only the particle extinction coefficient is left as unknown, so it can be calculated. The particle backscatter coefficient is then obtained from a ratio of elastic and inelastic signals for height z and a reference height z_0 with negligible particle scattering. The overlap function cancels out, if it can be assumed that $O(z, \lambda_0) = O(z, \lambda_R)$. In particular, the assumption can be made for well adjusted lidar systems with equal optical paths in the elastic and Raman detection channels. This allows the calculation of the backscatter coefficient in the near range.

2.3.3 Shadowing and imaging effects

The center of the far-range telescope of MARTHA is shaded by the secondary telescope mirror and the folding mirror that directs the laser beam into the atmosphere along the telescope axis. This construction is called a mono-axial design. Signals from the near range cannot reach the detector due to this shadow effect. So to speak, the lidar is blind up to several 100 m and profiles of the optical properties cannot be determined for that range. Furthermore, the principles of optical imaging prevent that scattered light from low heights can be completely sampled on the photocathode, because the image of the scattering volume is blurry for such distances. The shadow and the imaging effect determine the overlap function of the system. Especially the extinction profile is highly sensitive to this effect and can only be calculated for a complete overlap. The influence of the overlap effect depends on the optical design of the lidar. For MARTHA it was found that above 2.5 km the influence is small, and a total overlap is reached above 4 km (*Müller*, 2010). Below 1.2 km the systematic error of MARTHA becomes so large, that even with a correction the calculation of extinction profiles is almost impossible.

The correction of the data used in this work is done with the help of overlap functions. They can be found theoretically through ray-tracing models, what requires a good understanding of the beam and receiver characteristics. An experimental approach is described in *Wandinger and Ansmann* (2002). The method is based on the measurement of the elastic-backscatter signal and an additional pure molecular backscatter signal. According to this procedure, several overlap functions were found by *Müller* (2010) for MARTHA based on measurements between 2009 and 2010. However, small changes in the alignment of the laser beam can lead to huge uncertainties in the overlap function, especially in the near range. Therefore, for the determination of the extinction profile below 1 km, a well-mixed boundary layer is assumed. Thus a constant profile of β and S can be assumed.

The previous considerations refer to the far-range telescope. Due to its larger field of view the near-range telescope provides backscatter profiles down to a height of about 100 m. The uncorrected extinction profile is obtained between 700 m and 3 to 5 km. With an overlap function it would be possible to derive a profile down to 400 m. It should be noted that signals above 3 to 5 km cannot be detected, because the signal-to-noise ratio becomes too small. However, at that distance data from the far-range telescope can be used. As mentioned before, the near-range telescope has been implemented in September 2011. Thus its characteristic is not well investigated yet and only a few measurements are available up to now.

2.4 Classification of aerosol types

In general, the classification of aerosols is rather difficult and depends on the application. The aerosol often does not only consist of one type, but is rather a mixture of several of them. In this work, five basic types are considered with typical values of the Ångström exponent, the lidar ratio, and the depolarization ratio given in Tab. 2.1:

- urban-industrial aerosol,
- smoke or combustion aerosol,
- marine aerosol,
- dust aerosol,
- volcanic aerosol (i.e. volcanic ash and a fine-mode fraction).

Table 2.1: Typical values of the Ångström exponent, the lidar ratio, and the depolarization ratio for different aerosol types according to *Müller et al.* (2007) and *Wandinger et al.* (2010).

Property	Urban	Marine	Dust	Combustion	Volcanic Ash
$\mathring{a}$	1.4–1.7	0.1–0.3	0.15–0.3	1.2–1.5	0–0.5
S [sr]	40–60	20–30	50–60	50–80	40–60
δ	0%–5%	2%–3%	30%–35%	<5 %	35%–40%

Urban-industrial aerosol mainly consists of emission particles from traffic and industry as well as particles that origin from precursor gases. They belong to the sub-micron size range, where the form of the particles does not matter much. Thus they hardly depolarize the laser light. There are several sources for such aerosols in Europe as well as in North America. Long-range transport allows the observation even of such intercontinental particles. In this work, a case of aerosol transport from East Europe is considered (see Section 5.1). One should be aware that this case also includes contributions from fires.

Combustion aerosol, which often originates from biomass burning, has a strong fine-mode contribution. It can be caused by natural wild fires within Europe, e.g., in the Ukraine or in the Mediterranean. Also, combustion aerosol from fires in the boreal forests in North America and Siberia can be transported to Europe. In addition, anthropogenic activity contributes to biomass burning through wood or crop burning. The properties of smoke particles can strongly vary dependent on the kind of burning and processes which occur during the transport, among these are hygroscopic growth, coagulation, and photochemical mechanisms (*Wandinger et al.*, 2010).

Marine aerosol particles belong to the coarse mode due to their hygroscopic behavior. They are mainly formed from sea-salt particles or dimethyl sulfide from phytoplancton. Because marine aerosol particles are soluble in water, they have a spherical form in a humid environment and thus a depolarization ratio close to zero. Only stations located near the sea can usually observe marine aerosol, e.g., at the coast of the North Atlantic, the North Sea, and the Baltic Sea as well as the Mediterranean Sea. The observation of pure, marine aerosol at land stations is rather difficult due to pollution on the transport way or specific coastal circulations.

Also dust particles contribute to the coarse mode. They are characterized by their nonsphericity and thus a high depolarization ratio. Over Europe, observed dust aerosol originates mostly from the Saharan desert. These events occur quite frequently with one to three times per month and the strongest influence over Southern Europe (*Bösenberg et al.* (2003)). However, Central Europe is still affected significantly and a respective case is evaluated in Section 5.2. The retrieval of microphysical properties of dust particles is usually difficult and contains uncertainties as the non-spherical particles require complex scattering calculations which have to be simplified.

Volcanic aerosol, here considered as one type, can be a mixture of different particles. In this work, volcanic ash which contributes to the coarse mode and a fine mode that can be caused by conversion of sulfur dioxide into sulfate particles are distinguished. During the transport, the amount of sulfate particles increases caused by oxidation, whereas the ash is removed by sedimentation and washout. Therefore, the classification of volcanic aerosol is a particular challenge. Tab. 2.1 only lists the properties of ash particles which are characterized by their nonsphericity, similar to dust. Sulfate particles usually do not depolarize. Furthermore, they have a larger lidar ratio and Ångström exponent than ash.

Chapter 3

Retrieval algorithm for combined lidar and sun photometer data

3.1 Motivation

With AERONET worldwide information about aerosols is available. Based on sun and sky radiance measurements aerosol optical, microphysical, and radiative properties are provided which allow an extensive characterization of particles in the atmosphere. Unfortunately, these parameters are not representative for a single aerosol layer, but refer to the whole atmosphere from the ground to the stratosphere. Altitude distributions of aerosol properties can be measured with lidar instruments, but the microphysical information content is limited. Therefore, it seems to be a promising approach to combine lidar and sun photometer data to obtain a detailed image of microphysical properties of aerosol layers in the atmosphere.

A combined lidar and sun photometer retrieval algorithm has been developed in a cooperation between the Institute of Physics Minsk (Belarus) and the Laboratoire d'Optique Atmosphérique Lille (France) (*Chaikovsky et al.*, 2008). It was tested with IfT data in the frame of this work. Based on an optimal-estimation technique, volume concentration profiles for two aerosol modes, fine-mode and coarse-mode particles, are retrieved on the basis of measured lidar and sun photometer data. In order to find the best fit for the concentration profiles, it is assumed that the measured data are random variables which follow a normal distribution. To get the best estimation, there is a demand for an optimal estimator. "Optimal" means that a minimum of the average error can be reached. In accordance to *Eadie et al.* (1971), the maximum-likelihood method is applied which is a unified approach in case of a normal distribution.

It should be mentioned that sometimes the retrieval algorithm is called an inversion process, but it is rather a fitting process. Although the parameters may be obtained on the basis of measured data, the underlying mathematical equations do not suggest an actual inversion algorithm. The retrieval is an optimization procedure following a statistical estimation theory. This is done numerically, but it does not include the inversion of a set of equations as it is the case, e.g., for the inversion with regularization of lidar backscatter and extinction coefficient data as proposed by *Müller et al.* (1998, 1999a,b).

3.2 Overview

The following considerations are based on the technical report by *Chaikovsky et al.* (2008). The main purpose of the retrieval algorithm is the calculation of height profiles of aerosol mode concentrations. The whole process is divided into four steps. In the first step, data bases of radiometric and lidar measurements have to be generated. Radiometric data are available through the AERONET website. The respective files contain microphysical properties retrieved from sky radiance measurements at four wavelengths (441, 670, 875, and 1020 nm). Details are described in Section 2.2.3. Input parameters for the retrieval algorithm are values of backscatter and extinction coefficients retrieved from the microphysical and radiative properties for the corresponding lidar wavelengths. To distinguish them from the lidar coefficients α and β, they are denoted with a and b for extinction and backscattering, respectively. Further, it is assumed that aerosols are separated in two fractions, fine-mode and coarse-mode particles. Fine-mode particles are defined by a radius smaller than 0.5 μm and coarse-mode particles by a radius bigger than 0.5 μm. The two modes are indicated in the following with f and c, respectively. Volume concentrations of the two aerosol fractions $V_{f,c}$ and the aerosol optical thickness τ_{aer} at 675 nm are also taken into account. Details about the underlying algorithm for the calculation of the single-scattering albedo and scattering-matrix elements, that lead to the derivation of a and b, can be found in Section 3.3.1.

The lidar database consists of raw, elastic lidar signals $P(\lambda, z)$. For this work, only data from MARTHA at IfT Leipzig are used. As there is usually a high time resolution of the measurements, there is a need to calculate an average signal which is representative for the considered time period. Furthermore, the overlap effect has to be corrected (see Section 2.3.3). Also, radiometric and lidar measurements should be synchronized in time. That is not obvious, because lidar measurements often take place at night time as there is less background noise. However, radiometric data are only obtained at daytime. Under certain circumstances, if the observations show that there is not much atmospheric variability, it is possible to combine also data taken in different time periods. For such an occurrence, the AOT can also be corrected under the assumption that the ratio of the two aerosol modes and the aerosol constitution are nearly constant.

The second step is the preparation of the input data for the retrieval algorithm. It refers mainly to the range-corrected and overlap-corrected lidar signals $P_c(\lambda, z)$, for which a reference point z_N, where particle backscattering should be small compared to molecular backscattering, and the respective reference value $P_c(\lambda, z_N)$ have to be defined. The index c indicates the corrected lidar signal in contrast to the raw signal $P(\lambda, z)$. Lidar signal preparation is described in Section 3.3.2. It is also necessary to calculate the lidar signal dispersion $\Omega_L(\lambda, z)$ and the dispersion of optical parameters, what can be found in detail in Section 3.4.3. The term dispersion – in statistics also called variability or variation – is used to describe the measurement error or the error of the estimation of the retrieved properties. Height profiles of molecular backscatter and extinction coefficients $\beta_{mol}(z)$ and $\alpha_{mol}(z)$, respectively, are also created in that step. With all these parameters an expression can be found, later referred to as functional Ψ, whose minimization is the crucial part of the retrieval algorithm. To get this functional, a basic set of equations is established and the maximum-likelihood method is applied. It contains functions which depend on lidar and photometer measurements as well as a function that describes limitations of smoothness of the profiles. Their derivation is discussed in Section 3.4.

In the third step, the actual calculation of the concentration profiles $C_f(z)$ and $C_c(z)$ is done. Minimization of the functional Ψ is carried out, which not only leads to optimized height distributions of aerosol fine-mode and coarse-mode particles, but also to an optimized backscatter ratio $R(z_N)$ at the reference point. $R(z_N)$ is an important parameter for the calibration of the measured lidar signal. The underlying numerical process is described in Section 3.5.

Finally, a database is created which contains measured and calculated lidar signals for the three wavelengths 355, 532, and 1064 nm as well as the height distributions of fine-mode and coarse-mode concentrations (see Section 3.6). Together with the values obtained from radiometric measurements, profiles of particle backscatter and extinction coefficients $\beta_{par}(\lambda, z)$ and $\alpha_{par}(\lambda, z)$ can be calculated. Their interpretation and the comparison with independently obtained results is another part of this work.

Figure 3.1 gives a survey of the structure of the retrieval algorithm with its different steps. In the following sections, the four steps of the retrieval process are described in more detail.

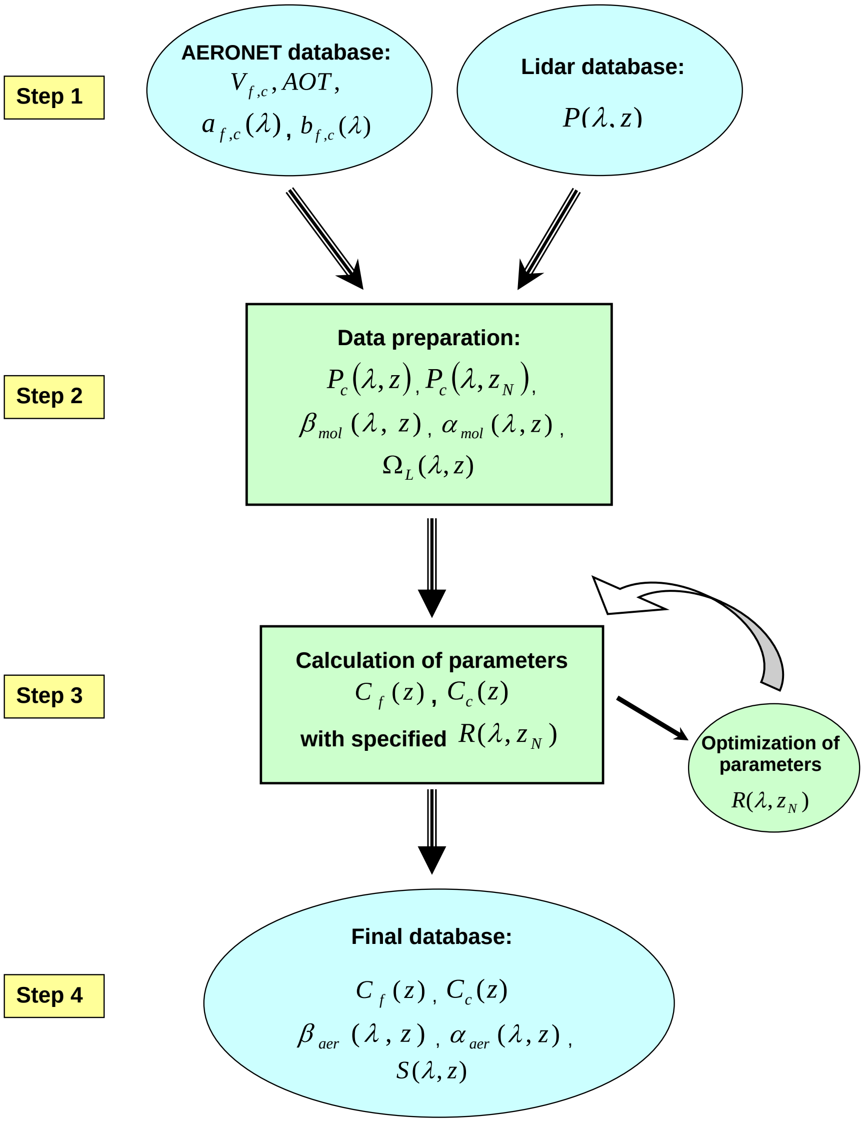

Figure 3.1: Structure of the retrieval algorithm. It consists of four steps which involve creation of radiometric and lidar databases, preparation of input data, calculation of the concentration profiles, and creation of the final database.

3.3 Databases and data preparation

3.3.1 Backscatter and extinction coefficients from sun photometer

For the combination of lidar and radiometric measurements, backscatter and extinction coefficients at the three lidar wavelengths have to be retrieved from microphysical properties obtained with the AERONET inversion algorithm described in Section 2.2.3. In order to get the coefficients, radiative aerosol properties such as the single-scattering albedo and scattering-matrix elements need to be calculated. This can be done by solving the vector radiative-transfer equation for a plane-parallel multi-layered atmosphere. A program to examine these properties for aerosols consisting of randomly oriented spheroids was developed by *Dubovik et al.* (2006).

In the AERONET inversion algorithm the complex refractive index, the size distribution, and the percentage of spherical particles are obtained for the four wavelengths of sky radiance measurements (441, 675, 870, and 1020 nm). Together with measurement information such as date, time, and julian day these parameters are used as input parameters for the program. From that the following properties are retrieved for the three lidar wavelenghts 355, 532, and 1064 nm:

- real and imaginary part of complex refractive index n_r and n_i,
- extinction, absorption, and scattering optical thickness τ_{ext}, τ_{abs}, and τ_{sca}, respectively,
- single-scattering albedo $\omega = \frac{\tau_{sca}}{\tau_{ext}}$,
- measuring angle Θ with $\Theta = 180°$ as standard,
- ratios of scattering-matrix elements of scattering matrix $F(\Theta)$:
  $F_{11}(\Theta)$, $\frac{F_{12}}{F_{11}}$, $\frac{F_{22}}{F_{11}}$, $\frac{F_{33}}{F_{11}}$, $\frac{F_{34}}{F_{11}}$ and $\frac{F_{44}}{F_{11}}$.

It is possible to gain these values not only for the total distribution of the aerosol, but also for fine-mode and coarse-mode particles. This is done by manipulating the size distribution in such a way that at a cut-off radius of 0.5 μm the respective mode is set to zero. Thus for the calculation of the fine-mode properties, the number concentration of aerosol particles with a radius $r > 0.5$ μm is assumed to be zero and vice versa.

It should be noted that the parts of the refractive index are calculated by linear approximation for wavelengths between 441 and 1020 nm. If $\lambda < 441$ nm or $\lambda > 1020$ nm, the refractive index equals the values for 441 and 1020 nm, respectively. More details about the theoretical model that is used in the program can be found in *Dubovik et al.* (2006). It includes the numerical integration over the volume size distribution and requires the parameterization of scattering and extinction cross sections. The scattering simulations are done by use of Lorenz-Mie calculations.

Finally, values of backscatter and extinction coefficients b and a can be obtained for the different wavelengths λ for both fractions:

$$b_{f,c}(\lambda) = 0.001 \frac{B_{f,c}(\lambda)}{V_{f,c}}, \tag{3.1}$$

$$a_{f,c}(\lambda) = 0.001 \frac{\tau_{ext_{f,c}}(\lambda)}{V_{f,c}}, \tag{3.2}$$

where $V_{f,c}$ are the volume concentrations of the fine-mode and coarse-mode particles which can be obtained from sun photometer measurements in accordance to Eq. (2.7), and

$$B_{f,c}(\lambda) = \frac{\tau_{ext}(\lambda)}{S_{f,c}(\lambda)}. \tag{3.3}$$

$S_{f,c}(\lambda)$ denotes the lidar ratio which is calculated in the following way:

$$S_{f,c}(\lambda) = \frac{4\pi}{\omega_{f,c}(\lambda) F_{11,f,c}(\lambda, \Theta = 180^\circ)}. \tag{3.4}$$

The factor of 0.001 in Eq. (3.1) and (3.2) is chosen in order to express the units of b and a in km^{-1} when $V_{f,c}$ is given in μm^3/μm^2. The recalculated parameters b and a represent mean values of the aerosol backscattering and extinction, respectively in the vertical column. They are only approximated values and, as randomly orientated spheroids are assumed in the model, especially the computations for non-spherical particles are critical and can contain errors.

3.3.2 Lidar signal

The raw lidar signals have to be prepared for the retrieval algorithm, because there is a demand for some corrections of the raw data and a synchronization with the radiometric measurements. At IfT Leipzig lidar measurements are carried out with a multi-wavelength Raman lidar, but only the elastic signals are used for the retrieval. First of all, the overlap effect is corrected by use of corresponding overlap functions. *Müller* (2010) analyzed lidar measurements at Leipzig between 2000 and 2010 and could work out different overlap functions depending on the status of the system. For each case in this work, the respective best fit was taken.

The time resolution of the lidar measurements is usually 30 seconds. As there is no demand for such a high time resolution, data are averaged over ten minutes, what also reduces the amount of data and the noise. In a next step, the background is removed from the data and the 10-minute averages are "synthesized". Based on the averaged signals the synthesizing process implies the calculation of a single signal for each wavelength that is representative for the entire time period which is examined. This final signal is interpolated to a grid with a height resolution of 15 m. If the lidar measurements were carried out under varying zenith angles and fields of view, that is taken into account in the synthesizing process. Furthermore, height sections with clouds have to be removed from the lidar signals as the radiometric data only refer to clear-sky measurements.

Finally, the lidar signal dispersion as a value for the measurement error is calculated. It is considered that the measured signal $P(z, \lambda)$ for wavelength λ consists of the real magnitude of the signal P_{real}, the non-synchronous noise P_q, the synchronous noise P_u, the background signal P_B, and a non-linear deviation ΔP:

$$P(z, \lambda) = P_{real} + P_q + P_u + P_B + \Delta P. \tag{3.5}$$

Non-synchronous noise shows up as dark and fluctuation currents of the photo receivers or as random noise at a time that is not synchronized with the moment of sending the laser pulse. The synchronous part describes noise that is caused while the backscattered light is directed to the receiving channels. Also internal noise in the registration system counts to that. The non-linear deviation is due to non-linear response of the receiving channels and defined by their technical properties. Explicit expressions can be found in *Chaikovsky et al.* (2008).

In this work, it is assumed that both synchronous and non-synchronous noise as well as the non-linear deviation can be neglected. These errors refer rather to analog signals than to digital photon counting which is the recording method used for MARTHA. Also, the error of the background signal is negligible as the background signal itself is sufficiently large. The dispersion is then written as

$$\frac{\langle \delta^2 P(z, \lambda) \rangle}{P(z, \lambda)^2} = \frac{\langle \delta^2 P_{real}(z, \lambda) \rangle}{P_{real}(z, \lambda)^2}. \tag{3.6}$$

The error is only caused by the signal noise which is expressed in terms of the mean squared error. As the retrieval is based on the maximum-likelihood method, it is necessary to quantify the variance. It is given by the mean squared error which accounts for the difference between the estimated and the real values. The optimization process is then done within the error margins.

3.3.3 Dispersion of optical parameters

While calculating the lidar signal dispersion also the dispersion of certain optical parameters is determined. That is in particular the error of the molecular optical thickness τ_{mol} as well as the error of the aerosol optical thickness τ_{aer} and the error of the total backscatter coefficient β. Similar to the error of the lidar signal, the errors of the optical parameters are expressed through the mean squared error:

$$\frac{\langle \delta^2(\tau_{mol}) \rangle}{\tau_{mol}^2} = c_1^2, \tag{3.7}$$

$$\frac{\langle \delta^2(\tau_{aer}) \rangle}{\tau_{aer}^2} = c_2^2, \tag{3.8}$$

$$\frac{\langle \delta^2(\beta) \rangle}{\beta^2} = c_3^2. \tag{3.9}$$

Constant values c_1^2, c_2^2, and c_3^2 are used here which have to be estimated realistically (see Chapter 4).

3.4 Basic set of equations

3.4.1 Basic functional

The basic set of equations consists of three functions which contain measured and calculated lidar signals, backsacatter and extinction parameters of the aerosol layer derived from radiometric measurements, and limitations of smoothness for the concentration profiles. The measured signals are denoted with an asterisk and are written as vectors $\mathbf{L}^*$ for the lidar data and $\mathbf{W}^*$ for the sun photometer data. They are subject to some uncertainty $\mathbf{\Delta}_L$ and $\mathbf{\Delta}_W$, respectively (*Dubovik and King*, 2000). In combination with the calculated signals $\mathbf{L}$ and $\mathbf{W}$ they can be expressed as follows:

$$\mathbf{L}^*(\lambda, z, P) = \mathbf{L}(\lambda, C_{f,c}(z), z) + \mathbf{\Delta}_L(\lambda, z), \tag{3.10}$$

$$\mathbf{W}^*(V_{f,c}) = \mathbf{W}(C_{f,c}(z)) + \mathbf{\Delta}_W. \tag{3.11}$$

Eq. (3.10) represents the function of the measured lidar signal $\mathbf{L}^*$ dependent on the wavelength λ, distance z, and the actual sounding signal P. The calculated lidar signal $\mathbf{L}$ is determined by the aerosol mode concentrations $C_{f,c}$. $\mathbf{\Delta}_L(\lambda, z)$ is the deviation between $\mathbf{L}^*$ and $\mathbf{L}$. Similarly, $\mathbf{W}^*$ contains the volume concentration $V_{f,c}$ of fine-mode and coarse-mode particles measured with the sun photometer, while $\mathbf{W}$ is calculated from the concentration profiles. $\boldsymbol{\Delta}_W$ denotes the differences between measured and calculated concentrations.

Smoothness constraints are necessary in order to get a stable solution as the retrieval algorithm is an ill-posed problem (*Tikhonov and Arsenin*, 1977). Such problems are characterized by incomplete available information and non-unique solutions. Furthermore, the solutions tend to depend not continuously on the input data. Even small uncertainties can produce large differences in the results. By use of *a priori* constraints unrealistic oscillations are eliminated and the solution can be derived successfully (*Twomey*, 1977). For the retrieval described in this work a technique is chosen that restricts the differences between the elements a_i of a vector $\mathbf{a} = [a_i]$ rather than the actual values. Thus it is assumed that the norm of the ith derivatives of the retrieved concentrations $C_{f,c}(z)$ are limited as follows (*Dubovik and King*, 2000):

$$\begin{aligned} a_i &= \int \left(\frac{\mathrm{d}^i C_{f,c}(z)}{\mathrm{d}^i z} \right)^2 \mathrm{d}z \approx \sum_{n=1}^{N} \left(\frac{\Delta^i C_{f,c}(z_n)}{(\Delta z)^i} \right)^2 \Delta z \\ &= (\Delta z)^{-2i+1} \mathbf{C}_{f,c}^T (\mathbf{G}_i)^T (\mathbf{G}_i) \mathbf{C}_{f,c}. \end{aligned} \tag{3.12}$$

$\Delta^i C_{f,c}(z_n)$ is the ith difference with $i = (1, 2, 3 \ldots)$. $\mathbf{C}_{f,c}$ are the concentration functions, and $\mathbf{G}_i$ denotes a matrix. The high-ranking T indicates their transposes.

In aerosol applications smoothing is most commonly done by use of second derivatives (*King et al.*, 1978; *King*, 1982; *Nakajima et al.*, 1996). For $i = 2$, differences $\Delta^i C_{f,c}(z_n)$ then take the form:

$$\Delta^2 C_{f,c}(z_n) = \Delta^1 C_{f,c}(z_n) - \Delta^1 C_{f,c}(z_{n+1}) = C_{f,c}(z_n) - 2C_{f,c}(z_{n+1}) + C_{f,c}(z_{n+2}). \tag{3.13}$$

The coefficients given by $\mathbf{G}_2$ allow the calculation of a vector $\mathbf{d}^2$ consisting of elements $\Delta^2 C_{f,c}(z_n)$:

$$\mathbf{d}^2 = \mathbf{G}_2 \mathbf{C}_{f,c}. \tag{3.14}$$

It is assumed that the derivative approaches zero with some deviations $\boldsymbol{\Delta}_{d_2}$:

$$\mathbf{d}^2 = \mathbf{0}^* - \boldsymbol{\Delta}_{d_2}. \tag{3.15}$$

Finally, the smoothness function can be written in the form

$$\mathbf{0}^*{}_{f,c} = \mathbf{G}_2 \mathbf{C}_{f,c} + \boldsymbol{\Delta}_{0,f,c}. \tag{3.16}$$

These constraints are effective in avoiding strongly oscillating solutions. Especially the use of the zero vector $\mathbf{0}^*$ for the derivatives of the concentrations eliminates this unrealistic effect (see *Dubovik and King* (2000) and *Dubovik* (2004) for more details).

After all data and their accuracy are taken into account, the retrieval algorithm searches for the best fit of the altitude distributions of fine-mode and coarse-mode concentrations. As mentioned before, principles of a statistical estimation theory are applied to define the optimization process (see Section 3.1). It is considered that the functions of Eq. (3.10), Eq. (3.11), and Eq. (3.16) are independent random variables. Following the law of normal distribution, the normal probability density function for the sum of the three functions is written in the form

$$P(\mathbf{C}_{f,c} \mid \mathbf{L}^*, \mathbf{W}^*) \propto \exp \left\{ -\frac{1}{2} \left\{ \begin{array}{l} \sum_{n=1}^{N-1} \sum_{j=1}^{J} (\mathbf{L}^*(\lambda_j, z_n) - \mathbf{L}(\lambda_j, z_n, \mathbf{C}_{f,c}))^T \times \\ \mathbf{\Omega}_L^{-1} (\mathbf{L}^*(\lambda_j, z_n) - \mathbf{L}(\lambda_j, z_n, \mathbf{C}_{f,c})) + \\ \sum_{n=1}^{N} (\mathbf{W}^* - \mathbf{W}(\mathbf{C}_{f,c}(z_n)))^T \times \\ \mathbf{\Omega}_W^{-1} (\mathbf{W}^* - \mathbf{W}(\mathbf{C}_{f,c}(z_n))) + \frac{A_{f,c}^2}{\sigma_{f,c}^2} \end{array} \right\} \right\} \tag{3.17}$$

where $\mathbf{\Omega}_L$ and $\mathbf{\Omega}_W$ are covariance matrices of the differences $\mathbf{\Delta}_L$ and $\mathbf{\Delta}_W$ (see chapter 3.4.3 for more details on their estimation).

It follows from Eq. (3.12) that $A_{f,c}^2$ can be calculated such that

$$A_{f,c}^2 = \sum_{n=1}^{N} \left(\frac{\Delta^2 C_{f,c}(z_n)}{(\Delta z_n)^3} \right)^2, \tag{3.18}$$

and $\sigma_{f,c}^2$ denotes the dispersion of the finite differences of $\mathbf{C}_{f,c}$.

Now the maximum-likelihood method is used in order to find the best estimate of the prospected parameters. According to *Eadie et al.* (1971) the solution retrieved by this approach is statistically the best as the errors have the smallest deviations. Applying the method means maximizing the probability density function Eq. (**??**). This can be achieved by finding the minimum of the quadratic expression in the exponent. That leads to the following basic functional Ψ, whose minimization is the main idea of the retrieval algorithm:

$$\begin{aligned} &\Psi(\mathbf{L}^*, \mathbf{W}^*, \mathbf{C}_{f,c}) = \\ &\quad \sum_{n=1}^{N-1} \sum_{j=1}^{J} [\mathbf{L}^*(\lambda_j, z_n) - \mathbf{L}(\lambda_j, z_n, \mathbf{C}_{f,c})]^T \mathbf{\Omega}_L^{-1} [\mathbf{L}^*(\lambda_j, z_n) - \mathbf{L}(\lambda_j, z_n, \mathbf{C}_{f,c})] + \\ &\quad \sum_{n=1}^{N} [\mathbf{W}^* - \mathbf{W}(\mathbf{C}_{f,c}(z_n))]^T \mathbf{\Omega}_W^{-1} [\mathbf{W}^* - \mathbf{W}(\mathbf{C}_{f,c}(z_n))] + \frac{A_{f,c}^2}{\sigma_{f,c}^2} \\ &\quad = \Psi_1(\mathbf{L}^*, \mathbf{C}_{f,c}(z_n)) + \Psi_2(\mathbf{W}^*, \mathbf{C}_{f,c}(z_n)) + \Psi_3(\mathbf{C}_{f,c}(z_n)). \end{aligned} \tag{3.19}$$

The basic functional consists of three terms, each of them containing certain requirements. The first term demands conformity of the measured and calculated lidar data, while the second one asks for consistency between radiometric measurements and the retrieved concentration profiles. The smoothness constraints discussed above are described by the last part of the functional.

It should be noted that Eq. (3.18) is only an expression to assure for accuracy in the retrieval process. More information about the minimization procedure, which is a technical question and can be done by different approaches, can be found in Section 3.5. The actual calculation of the parameters and the underlying equations will be discussed in more detail in the following sections.

3.4.2 Lidar equation

By analogy to Eq. (2.14), the elastic-backscatter signal for wavelength λ from a height z can be described in the following way:

$$P_c(\lambda, z) = E[\beta_{aer}(\lambda, z) + \beta_{mol}(\lambda, z)] \exp\left[-2(\tau_{aer}(\lambda, z) + \tau_{mol}(\lambda, z))\right], \tag{3.20}$$

where

$$P_c(\lambda, z) = \frac{P(\lambda, z) z^2}{P_0(\lambda)} \tag{3.21}$$

is the range-corrected and normalized lidar signal and E the system function.

The system function E can be defined by calibration. For that purpose, usually signal values from layers in the upper troposphere are taken as there is no significant influence by aerosols. In the following this height is called the reference point z_N. Thus it follows from Eq. (3.19):

$$P_c(\lambda, z_N) = E\left[\beta_{aer}(\lambda, z_N) + \beta_{mol}(\lambda, z_N)\right] \exp\left[-2(\tau_{aer}(\lambda, z_N) + \tau_{mol}(\lambda, z_N))\right], \tag{3.22}$$

and further:

$$E = \frac{P_c(\lambda, z_N)}{R(\lambda, z_N)\beta_{mol}(\lambda, z_N) T_N^2(\lambda)}, \tag{3.23}$$

where

$$R(\lambda, z_N) = \frac{\beta_{aer}(\lambda, z_N) + \beta_{mol}(\lambda, z_N)}{\beta_{mol}(\lambda, z_N)} \tag{3.24}$$

is the backscatter ratio at the reference point. As an initial value, it is assumed to be 1.1, which means there is 10% particle backscattering with respect to molecule backscattering. During the retrieval process the backscatter ratio is optimized, so that the wavelength dependence is retained.

$$T_N(\lambda) = \exp\left[-(\tau_{aer}(\lambda, z_N) + \tau_{mol}(\lambda, z_N))\right] \tag{3.25}$$

is the atmospheric transmission between ground and the reference point. It can be determined by the sun photometer, if the aerosol AOT is negligible above z_N.

The above expression for the system function might be not the most accurate one as the signal noise above z_N usually becomes quite large. Furthermore, $R(\lambda, z_N)$ is wavelength dependent. However, in the retrieval algorithm E is one of the optimizing variables and therefore, it is convenient to use $R(\lambda, z_N)$ as an optimization parameter.

In the retrieval program the measured lidar signal is reconstructed for every height step z_n and wavelength λ from the corrected lidar signals $P_c(z_n)$. Also, a second lidar signal is calculated from the radiometric parameters of backscatter and extinction coefficients together with the concentration profiles. To get expressions for the reconstructed signal as well as the calculated one, Eq. (3.22) is inserted into Eq. (3.19), which then takes the following form:

$$\begin{aligned} P_c(\lambda, z_n) = {} & \frac{P_c(\lambda, z_N)}{R(\lambda, z_N)\beta_{mol}(\lambda, z_N)T_N(\lambda)^2} \\ & \times \left(\beta_{aer}(\lambda, z_n) + \beta_{mol}(\lambda, z_n)\right) \exp\left[-2(\tau_{aer}(\lambda, z_n) + \tau_{mol}(\lambda, z_n))\right]. \end{aligned} \tag{3.26}$$

Substituting $T(z_N)$ and rearranging leads to:

$$\begin{aligned} & \frac{P_c(\lambda, z_n)}{P_c(\lambda, z_N)} R(\lambda, z_N)\beta_{mol}(\lambda, z_N) \exp\left[-2(\tau_{mol}(\lambda, z_N) - \tau_{mol}(\lambda, z_n))\right] = \\ & \left(\beta_{aer}(\lambda, z_n) + \beta_{mol}(\lambda, z_n)\right) \exp\left[-2(\tau_{aer}(\lambda, z_n) - \tau_{aer}(\lambda, z_N))\right]. \end{aligned} \tag{3.27}$$

With

$$\tau(z_n, z_N) = \tau(z_N) - \tau(z_n), \tag{3.28}$$

it follows:

$$\begin{aligned} & \frac{P_c(\lambda, z_n)}{P_c(\lambda, z_N)} R(\lambda, z_N)\beta_{mol}(\lambda, z_N) \exp\left[-2\tau_{mol}(\lambda, z_n, z_N)\right] = \\ & \left(\beta_{aer}(\lambda, z_n) + \beta_{mol}(\lambda, z_n)\right) \exp\left[2\tau_{aer}(\lambda, z_n, z_N)\right]. \end{aligned} \tag{3.29}$$

The left-hand side of Eq. (3.28) can be taken as the function of the measured lidar signal $\mathbf{L}^*$ and the right-hand side can be used to calculate the lidar signal $\mathbf{L}$:

$$\mathbf{L}^*(\lambda, z_n) = \frac{P_c(\lambda, z_n)}{P_c(\lambda, z_N)} R(\lambda, z_N)\beta_{mol}(\lambda, z_N) \exp\left[-2\tau_{mol}(\lambda, z_n, z_N)\right], \tag{3.30}$$

$$\mathbf{L}(\lambda, z_n) = \left(\beta_{aer}(\lambda, z_n) + \beta_{mol}(\lambda, z_n)\right) \exp\left[2\tau_{aer}(\lambda, z_n, z_N)\right]. \tag{3.31}$$

For the calculation of **L** radiometric data are taken into account such that β_{aer} and τ_{aer} are calculated from the mean values of the backscatter and extinction coefficients found before (see Eq. (3.1) and (3.2)). Together with the concentration for fine-mode and coarse-mode particles, for every height step z_n recalculated backscatter and extinction coefficients can be derived. As mentioned earlier τ_{aer} is the integral over α_{aer} (see Eq. (2.13)). The following expressions are used to get β_{aer} and α_{aer} (*Chaikovsky et al.*, 2008):

$$\beta_{aer}(\lambda, z_n) = C_f(z_n) b_f(\lambda) + C_c(z_n) b_c(\lambda), \tag{3.32}$$

$$\alpha_{aer}(\lambda, z_n) = C_f(z_n) a_f(\lambda) + C_c(z_n) a_c(\lambda). \tag{3.33}$$

It should be noted that radiometric measurements are representative for the whole column of the atmosphere, while due to the overlap effect during lidar measurements (see Section 2.3) no data are available for the lower layers. Therefore, it is assumed that up to a height z_{N_0} the atmosphere is homogeneous. The concentration equals $C_{f,c}(z_{N_0})$ for $z < z_{N_0}$, and α_{aer} and β_{aer} are constant in that range.

Finally, equations (3.29) to (3.32) give an expression for Ψ_1 in Eq. (3.18):

$$\Psi_1(\mathbf{L}^*, \mathbf{C}_{f,c}(z_n)) = \tag{3.34}$$

$$\sum_{n=N}^{N_0} \sum_{j=1}^{J} \left\{ \begin{array}{l} \mathbf{L}^* - (C_f(z_n) b_f(\lambda_j) + C_c(z_n) b_c(\lambda_j) + \beta_{mol}(\lambda_j, z_N)) \\ \times \exp\left(-2 \sum_{i=N}^{i=n+1} (C_f(z_i) a_f(\lambda_j) + C_c(z_i) a_c(\lambda_j) \Delta z_i) \right) \end{array} \right\}^2 \frac{k_j^2}{\Omega_L^j(z_n)}.$$

The calculation starts at the reference point z_N and goes downward to z_{N_0}. Therefore, $\Delta z_i = z_{i-1} - z_i < 0$ is defined in order to move in the opposite direction of the z-axis. Furthermore, k_j^2 is used as a regularization parameter, and $\Omega_L^j(z_n)$ denotes weight coefficients which are dependent on measurement errors as well as on aerosol layer parameters. Their estimation follows from the elements of the covariance matrix $\mathbf{\Omega_L}$ which is considered in the next chapter. The function $\mathbf{L}^*$ is expressed as follows:

$$\mathbf{L}^*(\lambda_j, z_n) = \frac{P_c(\lambda_j, z_n)}{P_c(\lambda_j, z_N)} R(\lambda_j, z_N) \beta_{mol}(\lambda_j, z_N) \exp\left(2 \sum_{i=N}^{n+1} \alpha_{mol}(\lambda_j, z_i) \Delta z_i \right). \tag{3.35}$$

3.4.3 Estimation of the covariance matrix

Covariance matrices were introduced in Eq. (**??**). Now a closer look at $\mathbf{\Omega}_L$ is taken. It is the covariance matrix of differences $\mathbf{\Delta}_L(\lambda, z_n) = \mathbf{L}^*(\lambda, z_n) - \mathbf{L}(\lambda, \mathbf{C}_{f,c}(z_n), z_n)$. Thus the diagonal elements of $\mathbf{\Omega}_L$ represent the dispersion of differences between calculated and measured lidar signals dependent on height z_n or, in other words, the squared uncertainties. It follows from Eq. (3.29) and Eq. (3.30) that

$$\begin{aligned} \mathbf{\Delta}_L(\lambda, z_n) = \quad & \mathbf{L}^*(\lambda, z_n) - \mathbf{L}(\lambda, \mathbf{C_{f,c}}(z_n), z_n) \\ = \quad & \frac{P_c(\lambda, z_n)}{P_c(\lambda, z_N)} R(\lambda, z_N)\beta_{mol}(\lambda, z_N) \exp\left[-2\tau_{mol}(\lambda, z_n, z_N)\right] - \\ & (\hat{\beta}_{aer}(\lambda, z_n) + \beta_{mol}(\lambda, z_n)) \exp\left[2\hat{\tau}_{aer}(\lambda, z_n, z_N)\right], \end{aligned} \tag{3.36}$$

where $\hat{\beta}_{aer}$ and $\hat{\tau}_{aer}$ are estimations of the aerosol backscatter coefficient and the aerosol optical thickness, respectively.

An error estimation $\delta_L(\lambda, z_n)$ for the difference can be derived from measurement errors in the lidar signal P_c as well as errors in the optical parameters $\beta_{aer,mol}$ and τ_{aer}:

$$\begin{aligned} \delta_L(\lambda, z_n) = \quad & \delta\mathbf{\Delta}_L(\lambda, z_n) \\ = \quad & -2\mathbf{L}^*(\lambda, z_n)\delta(\tau_{mol}(\lambda, z_n)) + \mathbf{L}^*(\lambda, z_n)\frac{\delta(P_c(\lambda, z_n))}{P_c(\lambda, z_n)} \\ & - \exp[2\hat{\tau}_{aer}(\lambda, z_n, z_N)]\delta(\hat{\beta}) - 2\exp[2\hat{\tau}_{aer}(\lambda, z_n, z_N)]\hat{\beta}\delta(\hat{\tau}_{aer}), \end{aligned} \tag{3.37}$$

with $\hat{\beta} = \hat{\beta}_{aer} + \beta_{mol}$ as estimation of the total backscatter coefficient.

Finally, to get $\mathbf{\Omega}_L$, the covariance $\langle\delta_L(\lambda, z_n)\delta_L(\lambda, z_n)\rangle$ has to be calculated and it takes the form:

$$\begin{aligned} \mathbf{\Omega}_L(\lambda, z_n) = \quad & \langle\delta_L(\lambda, z_n)\delta_L(\lambda, z_n)\rangle \\ = \quad & 4(\mathbf{L}^*(\lambda, z_n))^2\langle\delta^2(\tau_{mol}(\lambda, z_n))\rangle + (\mathbf{L}^*(\lambda, z_n))^2\frac{\langle\delta^2(P_c(\lambda, z_n))\rangle}{(P_c(\lambda, z_n))^2} \\ & + \exp[4\hat{\tau}_{aer}(\lambda, z_n, z_N)]\langle\delta^2(\hat{\beta})\rangle + 4\exp[4\hat{\tau}_{aer}(\lambda, z_n, z_N)]\hat{\beta}^2\langle\delta^2(\hat{\tau}_{aer})\rangle. \end{aligned} \tag{3.38}$$

Assumptions for the dispersion estimation have been discussed before (see Section 3.3.2 and 3.3.3). If one takes this into account, the second term of the right-hand side of Eq. (3.37) vanishes, constant coefficients c_1^2, c_2^2, and c_3^2 appear, and τ_{mol} is substituted by a sum over α_{mol}. Furthermore, it is assumed that $R_N = 1$ for the calculation of the weight coefficients $\Omega_L^j(z_n)$, so that

$$\begin{aligned} & \Omega_L^j(z_n) = \\ & 4\left[\frac{P_c(\lambda_j, z_n)}{P_c(\lambda_j, z_N)}\beta_{mol}(\lambda_j, z_N)\exp\left(2\sum_{i=N}^{n+1}\alpha_{mol}(\lambda_j, z_i)\Delta z_i\right)\right]^2 c_1^2\left(\sum_{i=N}^{n+1}\alpha_{mol}(\lambda_j, z_i)\Delta z_i\right)^2 \\ & + (\hat{\beta}(\lambda_j, z_n))^2\exp\left(4\overline{\tau_{aer}(\lambda_j)}\frac{z_N - z_n}{z_N}\right)\left[c_3^2 + 4c_2^2\left(\overline{\tau_{aer}(\lambda_j)}\frac{(z_N - z_n)}{z_N}\right)^2\right], \end{aligned} \tag{3.39}$$

where $\overline{\tau_{aer}}$ denotes an average value of the aerosol optical thickness measured by sun photometer. It is set to 0.2. Together with the term $\frac{z_N - z_n}{z_N}$ it gives an estimation of the AOT. It should be mentioned that values of $\Omega_L^j(z_n)$ are calculated while preparing the lidar data and not while running the actual retrieval algorithm because there are no parameters in Eq. (**??**) that need to be optimized.

3.4.4 Sun photometer equation

As mentioned before, volume concentrations of fine-mode and coarse-mode particles $V_{f,c}$ can be retrieved from radiometric measurements by inversion algorithms (see Section 2.2.3). They are integral values over the whole column of the atmosphere and used as parameters for $\mathbf{W}^* = V_{f,c}$ in Eq. (3.11). Again, it is considered that the concentration equals $C_{f,c}(z_{N_0})$ for $z < z_{N_0}$. Thus the function $\mathbf{W}$ for calculated concentrations can be written down as follows:

$$\mathbf{W}(\mathbf{C}_{f,c}(z_n)) = \sum_{n=N_0}^{N} (C_{f,c}(z_n)|\Delta z|) + C_{f,c}(z_{N_0})z_{N_0}, \tag{3.40}$$

where Δz is a constant height step. The functional Ψ_2 in Eq. (3.18) then takes the form:

$$\Psi_2(V_{f,c}, C_{f,c}(z_n)) = \frac{h_{f,c}^2}{\Omega_{f,c}} \left(V_{f,c} - \sum_{n=N_0}^{N} (C_{f,c}(z_n)|\Delta z_n|) - C_{f,c}(z_{N_0})z_{N_0} \right)^2, \tag{3.41}$$

where $h_{f,c}^2$ is a regularization parameter, and $\Omega_{f,c}$ is the error dispersion of $V_{f,c}$. The latter one remains unknown, thus the ratio

$$f_{f,c} = \frac{h_{f,c}^2}{\Omega_{f,c}} \tag{3.42}$$

is introduced and taken as a regularization parameter.

3.4.5 Smoothness equation

Smoothness constraints have been already discussed in Section 3.4.1. Second-order differences are used, and Eq. (3.17) is specified in the following way:

$$A_{f,c}^2 = \sum_{n=1}^{N} \frac{1}{(|\Delta z_n|)^3} (2C_{f,c}(z_n) - C_{f,c}(z_{n-1}) - C_{f,c}(z_{n+1}))^2. \tag{3.43}$$

That finally gives the third functional Ψ_3 in Eq. (3.18):

$$\Psi_3(V_{f,c}, C_{f,c}(z_n)) = \sum_{n=1}^{N} \frac{d^2_{f,c}}{(|\Delta z_n|)^3}(2C_{f,c}(z_n) - C_{f,c}(z_{n-1}) - C_{f,c}(z_{n+1}))^2, \tag{3.44}$$

with another regularization parameter $d^2_{f,c}$.

3.5 Optimization process

The basic functional Ψ was defined in detail in the previous sections. Again, it takes the following form:

$$\Psi(\mathbf{L}^*, V_{f,c}, \mathbf{C}_{f,c}, R(z_N)) = \Psi_1(\mathbf{L}^*, \mathbf{C}_{f,c}(z_n), R(z_N)) + \Psi_2(V_{f,c}, \mathbf{C}_{f,c}(z_n)) + \Psi_3(\mathbf{C}_{f,c}(z_n)), \tag{3.19}$$

where $\mathbf{C}_{f,c}$ and $R(z_N)$ are the parameters that should be determined by the retrieval algorithm and whose optimization lead to the minimum of the functional.

The calculation of the concentration profiles is based on a gradient method. It is a first-order optimization algorithm which uses the negative of the gradient of a function to find its minimum (*Press et al.*, 2007). To find the kth increment of the altitude distribution $C^k_{f,c}(z_n)$ in a certain height z_n, the partial derivatives of Ψ are calculated:

$$\frac{\partial \Psi(\mathbf{L}^*, V_{f,c}, \mathbf{C}_{f,c}, R(z_N))}{\partial C_{f,c}(z_n)} = F_{f,c}(\mathbf{L}^*, V_{f,c}, \mathbf{C}_{f,c}, R(z_N)). \tag{3.45}$$

The next approximation of $C^{k+1}_{f,c}$ is now found by moving along from $C^k_{f,c}$ in the direction of the gradient until a local minimum is reached:

$$C^{k+1}_{f,c}(z_n) = C^k_{f,c}(z_n) - F_{f,c}\frac{C^k_{f,c}}{m_{f,c}\sqrt{(F_f(z_n)^2) + (F_c(z_n)^2)}}, \tag{3.46}$$

with a parameter $m_{f,c} > 1$ that guarantees that the right-hand side of the above equation will always be smaller than the left-hand side. This is necessary in order to get a positive concentration distribution. Another constraint is the use of positive initial values $C^0_{f,c}(z_n)$. The process of increment calculation given by Eq. (3.39) continues until the change in $C^k_{f,c}(z_n)$ is sufficiently small. After calculation of the $C_{f,c}(z_n)$ values, $R(\lambda_j, z_N)$ is derived with the same method. Thus the partial derivatives of Ψ with respect to R are calculated:

$$\frac{\partial \Psi(\mathbf{L}^*, V_{f,c}, \mathbf{C}_{f,c}, R(z_N))}{\partial R(\lambda_j, z_N)} = F^j_R(\mathbf{L}^*, V_{f,c}, \mathbf{C}_{f,c}, R(z_N)). \tag{3.47}$$

Finally, dependent on the wavelength, values of the backscatter ratio at the reference point are derived:

$$R^{k+1}(\lambda_j, z_N) = R^k(\lambda_j, z_N) - F_R^j \frac{R^k(\lambda_j, z_N)}{m_j \sqrt{(F_R^1)^2 + (F_R^2)^2 + (F_R^3)^2}}. \tag{3.48}$$

This procedure guarantees that no falsified wavelength dependency is introduced in the calculations, because initially the backscatter ratio is assumed to be 1.1 for all wavelengths.

3.6 Final Database

After the retrieval is run, volume concentration profiles of fine-mode and coarse-mode particles are available as well as the measured and the calculated lidar signals. Besides the concentration distributions, the backscatter and extinction coefficients are the values of interest. Their recalculation follows from Eq. (3.31) and (3.32). The lidar ratio as the ratio of both quantities is then also given. In Chapter 5 the results of the retrieval algorithm are compared to results of other methods. In particular, backscatter profiles derived after the Klett–Ferald method are used for comparison.

The retrieval of microphysical particle properties from combined measurements of different instruments is a complex process. The previous sections covered not only the physical background, but also explained the underlying mathematical equations in detail which are essential for an overall understanding. Because it does not require much calculation time, the algorithm software represents a fast tool for the retrieval of microphysical particle properties. The next chapters present first test results based on selected cases which may contribute to a further improvement of the algorithm.

Chapter 4

Data preparation and evaluation tools

Within this work the retrieval algorithm was tested specifically in terms of its sensitivity to the overlap effect. It can be taken into account in different ways. Section 4.1 covers in particular the actual overlap correction as well as the consideration of the overlap effect while preprocessing the lidar data for the retrieval algorithm. Further, a survey about the whole data processing is given, including the creation of the final database.

Not only the data preparation and evaluation is important for the case studies, but also an overview about the meteorological background. Therefore, weather charts provided by the German Meteorological Service (Deutscher Wetterdienst – DWD) are used for an assessment of the synoptic situation. To get a brief overview about the aerosol layers so-called quicklooks are depicted. Quicklooks are time-height cross sections of the range-corrected 1064-nm signal from the MARTHA measurements. Thus the vertical layering of the atmosphere and its temporal development are apparent. To obtain detailed information about the type of aerosol, three different atmospheric transport models are considered which are explained in Section 4.2.

4.1 Data processing

The raw lidar data were overlap-corrected by use of proper overlap functions that were obtained by *Müller* (2010) through an analysis of lidar measurements carried out with MARTHA at Leipzig between 2009 and 2010. The overlap functions are shown in

Fig. **??**. Above 2.5 km they are all close to one. Between 700 m and 2.5 km there is a significant difference between the function of 28 June 2010 and the other three. As the functions of 12 January 2009, 7 December 2009, and 17 June 2010 have a similar shape, the function of 7 December 2009 was chosen as representative. The data considered in this work were corrected with this function and – for comparison and sensitivity tests – with the one of 28 June 2010. Finally, depending on the case, only one of the datasets was used for the retrieval.

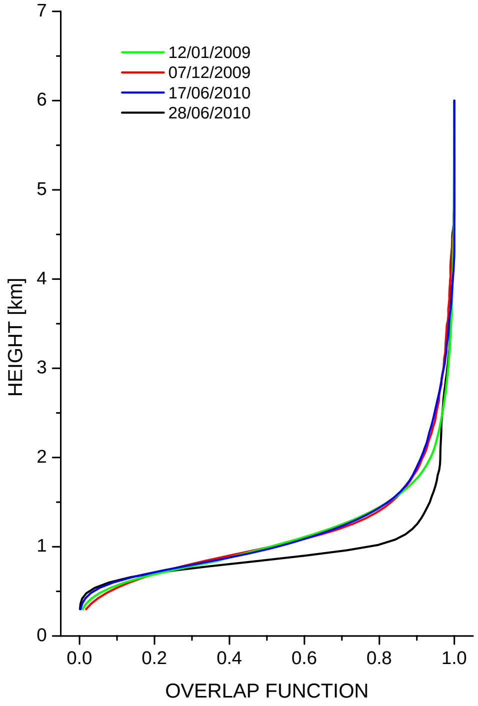

Figure 4.1: Profiles of the overlap function for different dates.

After the overlap correction the individual lidar profiles, accumulated over 30 s each, were averaged over the whole time period that was considered. In the next step, the lidar signal dispersion was calculated as described in Section 3.3.2 and normalized according to the value at the reference point. In the lidar data analysis vertical profiles of the molecular optical thickness and the molecular backscatter coefficient are calculated by means of atmospheric standard models. For this work, the U.S. standard atmosphere model was chosen. This might introduce large uncertainties in the calculations, because the values for temperature and pressure are fixed and cannot assimilated to the measurement conditions. The profiles for the molecular properties are required in the signal normalization procedure and to remove air-molecule-scattering effects in the determination of the particle extinction and backscatter coefficients. Parameters for the calculation of the lidar signal dispersion are listed in Tab. 4.1, see also Section 3.3.3 and 3.4.3.

Table 4.1: Parameters for the calculation of the lidar signal dispersion.

Parameter	Value	Equation
Relative error of τ_{mol}, c_1^2	0.03	3.7
Relative error of τ_{aer}, c_2^2	0.1	3.8
Relative error of β, c_3^2	0.03	3.9
Average value of the AOT $\overline{\tau_{aer}}$	0.2	3.39

The profiles of the normalized signal, the signal dispersion, the molecular optical thickness, and the molecular backscatter coefficient can be obtained for a defined range between the height z_{N_0} and a height that is above the reference point. Below z_{N_0} the volume concentration is hold constant at the value of z_{N_0}. This assumption usually works fine for a well-mixed boundary layer where only small variations in the retrieved properties are expected.

The sun photometer measurement was chosen in accordance to the lidar measurements. Therefore, the time of the radiometric observation usually lies within the time period of the lidar measurements. Radiometric data were retrieved as described in Section 3.3.1. The retrieval was then run leaving the algorithm parameters, these are in particular the regularization parameters, for the aerosol mode concentrations $f_{f,c}$ and for the smoothness constraints $\frac{d_{f,c}^2}{10^{-3}\Delta z^3}$ unchanged (see Tab. 4.2). Regularization parameters for the lidar signals k_j^2 were adjusted to achieve the best agreement between measured and calculated lidar signals.

According to Eq. (3.31) and (3.32) backscatter and extinction coefficients can be calculated from the retrieved aerosol mode concentrations for the three wavelengths. This allows a comparison with backscatter coefficients that were obtained using the Raman and the Klett method (see Section 2.3.2). Furthermore, the lidar ratio at 532 nm can be derived which is a useful parameter in order to classify aerosols. Thus for each case height profiles of the three backscatter and extinction coefficients as well as the lidar ratio at 532 nm and altitude distributions for both fine and coarse mode are shown in the following sections.

Table 4.2: Algorithm Parameters

Parameter	Value	Equation
Lidar signals		
k_{355}^2	$1 * 10^{-8} - 1 * 10^{-14}$	3.34
k_{532}^2	$1 * 10^{-8} - 4 * 10^{-14}$	3.34
k_{1064}^2	$1 * 10^{-8} - 1 * 10^{-14}$	3.34
Aerosol mode concentrations		
f_f	$4 * 10^{-6}$	3.42
f_c	$4 * 10^{-6}$	3.42
Smoothness of profiles		
$\frac{d_f^2}{10^{-3}\Delta z^3}$	$2.5 * 10^{-8}$	3.44
$\frac{d_c^2}{10^{-3}\Delta z^3}$	$5 * 10^{-8}$	3.44

4.2 Modeling tools

The **HY**brid **S**ingle-**P**article **L**agrangian **I**ntegrated **T**rajectory Model (HYSPLIT) is a model that not only computes simple air-parcel trajectories, but also can be used to carry out complex dispersion and deposition simulations of pollutants and hazardous material (*ARL-Homepage*, 2011). Furthermore, it allows the tracking and forecasting of different aerosol particles such as radioactive material, volcanic ash, and wildfire smoke. For that purpose, both the Lagrangian and the Eulerian approach are used together. The Lagrangian approach is based on a moving frame of reference and thus air parcels are followed from their initial location. This approach is applied to the calculation of advection and diffusion processes. The Eulerian method rather uses a fixed three-dimensional grid as the frame of reference, e.g., for pollutant concentrations. In this work, HYSPLIT is used to calculate backward trajectories to determine the origin of the aerosol particles. It is possible to compute multiple trajectories by use of meteorological variations. Also, certain meteorological variables along the trajectories can be displayed.

FLEXPART is another Lagrangian particle dispersion model that "computes trajectories of a large number of so-called particles (not necessarily representing real particles, but infinitesimally small air particles) to describe the transport and diffusion of tracers in the atmosphere" (*Stohl et al.*, 2005). Based on an observation in a certain layer, the transport of 50,000 particles is modeled (*Stohl et al.*, 1998; *Stohl and Thomson*, 1999). Only air parcels that traveled below 2000 m within the last 10 days before the observation are taken into account. The output is a plot that shows the integrated residence time in a geographical grid box. FLEXPART is used to model long-range and mesoscale transport as well as diffusion, dry and wet deposition, and radioactive decay of tracers. For this work, one is only interested in transportation which is calculated by resolved winds and parameterized subgrid motions.

To quantify especially the dust portion of the observed aerosol, the **D**ust **RE**gional **A**tmospheric **M**odel (DREAM) is used (*Nickovic et al.*, 2001). It is an atmospheric dust forecast system that is operated by the Earth Sciences Divison of the Barcelona Supercomputing Center. Based on an Euler-type partial differential non-linear equation for dust mass continuity, the atmospheric life cycle of eroded dust is predicted. All major processes of the atmospheric dust cycle are included, that are in particular the dust production scheme with introduced viscous sub-layer, soil wetness effects on dust production, dry deposition and below-cloud scavenging, horizontal and vertical advection, as well as turbulent and lateral diffusion. One of the key components is the modeling of the source term. Wind erosion of dust is determined by the type of soil and vegetation cover, soil moisture content, and surface atmospheric turbulence (*BSC-Homepage*, 2011). Furthermore, improvements in the latest version DREAM8b (*Pérez et al.*, 2006a,b) introduced arid and semiarid categories for the dust sources as well as the global soil texture data set for the evaluation of the particle sizes.

Examples of the calculations of HYSPLIT, FLEXPART, and DREAM are shown in the next sections. Besides the models for the determination of aerosol particle sources, further observation data can be used. In this work, firemaps based on measurements carried out with the **MOD**erate Resolution **I**maging **S**pectrometer (MODIS), mounted on the Terra and Aqua satellites, are used to obtain information about the occurrence of biomass burning and forest fires in the considered time period (*FIRMS-Homepage*, 2011).

Chapter 5

Case studies

Three cases were chosen to test the retrieval algorithm for different aerosol situations. Section 5.1 describes a case of East European aerosol which was transported to Leipzig and consisted mainly of fine-mode particles. The second case refers to a major Saharan dust outbreak in May 2008. During this episode a pure coarse-mode event was observed over Leipzig on 30 May 2008 (see Section 5.2). As it turned out the algorithm is rather sensitive to varying data in the range up to 1.5 km. Due to the overlap effect information about this range is difficult to access (see Section 2.3.3). The problem is tried to be solved by assuming a homogeneous atmosphere between ground and a height z_{N_0}. This height can be varied in order to find the best estimation of the concentration profiles. For the Saharan dust case, this procedure is explained in more detail. Furthermore, the two cases could be used for an error estimation of the concentration distributions as explained in Section 5.3.

The findings are applied to the third case which refers to the Eyjafjallajökull eruption on 14 April 2010. The aerosol observed over Leipzig on 19 April 2010 did not only consist of volcanic ash, but also of non-ash components (see Section 5.4). The distinction between different types of particles is a challenging task. Based on the separation between fine and coarse mode, in this work volcanic ash and non-ash particles are identified. This approach is compared with the method of *Ansmann et al.* (2011), who used depolarization ratios for the distinction.

5.1 Case of 6 April 2009

5.1.1 Meteorological situation and database

Due to the influence of high pressure, aerosol from East Europe was transported to Leipzig on 6 April 2009. The center of the high-pressure system was located over North Germany and Poland. Thus the air flow coming from Great Britain was first directed to Poland and East Europe before it reached Saxony from the south-east (see Fig. 5.1). Lidar measurements were carried out the whole day, but cirrus clouds were apparent for most of the time. For the evening period between 19:38 and 21:33 UTC backscatter profiles derived after the Raman method are available for comparison. Thus this period was selected for the case study. Because the aerosol properties obtained from radiometric measurements did not change much during the course of the day, and values of the size distribution of the aerosol particles were only retrieved in the afternoon, the corresponding values are based on the sun photometer measurement at 13:14 UTC.

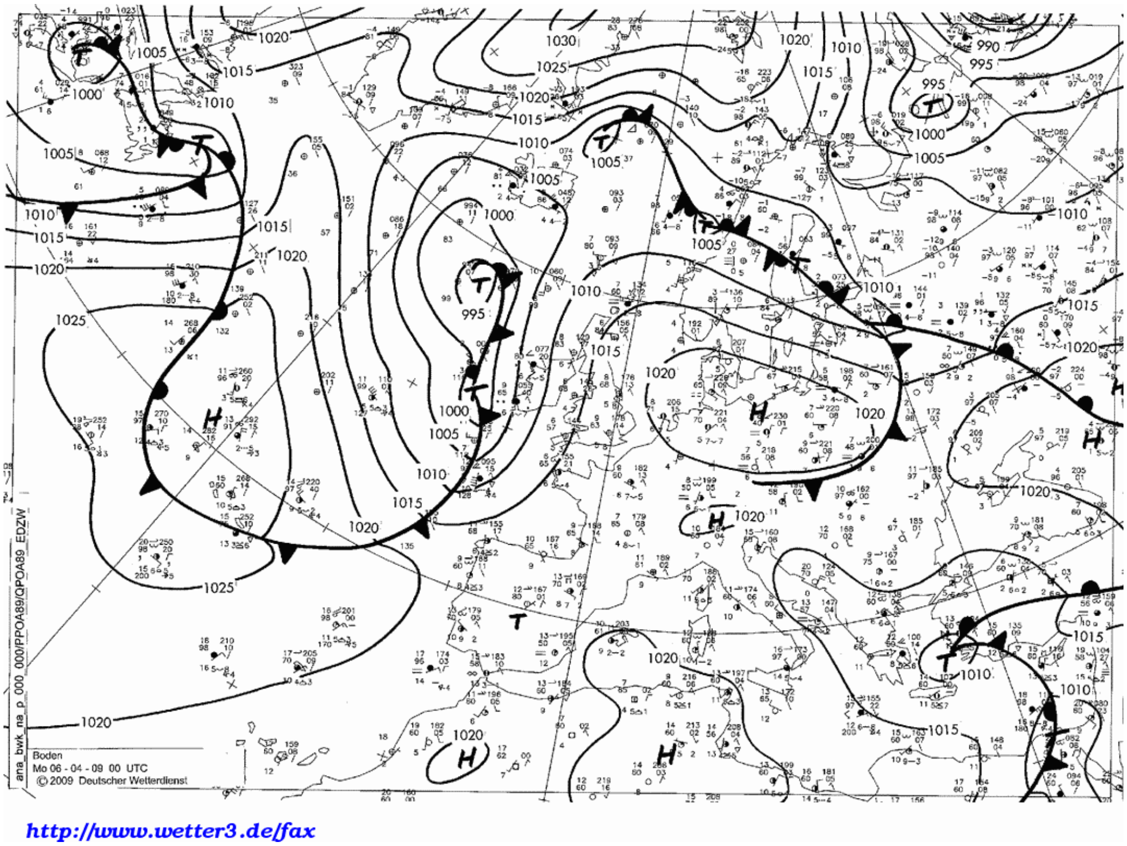

Figure 5.1: DWD-analysis weather chart for the ground level at 9 UTC on 6 April 2009.

The quicklook in Fig. 5.2 reveals the aerosol layer in the range between 0.5 and 3 km. The red color indicates a strong backscatter signal while blue stands for weak signals. It should be mentioned that the weaker backscatter signal below 0.5 km is due to the overlap effect. In that range aerosol is also located, but does not appear in the color plot. There is stronger backscattering between 1 and 1.5 km than between 1.5 and 3 km. Especially for such structures concentration profiles can provide information about the kind of the aerosol. Because of the cirrus clouds around a height of 10 km, the reference point for the calculations was chosen at 9 km, and lidar signals above the reference point were neglected.

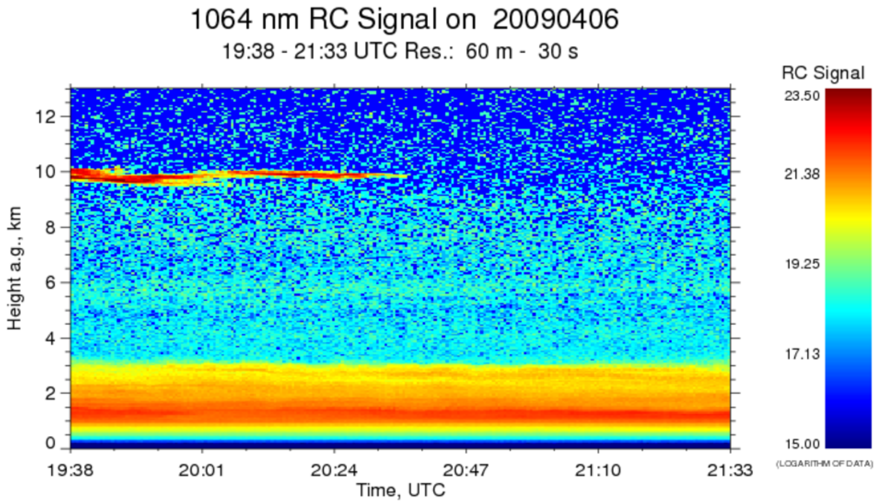

Figure 5.2: Range-corrected signal at 1064 nm between 19:38 and 21:33 UTC on 6 April 2009. Spatial resolution is 60 m and time resolution is 30 s.

The size distribution obtained from the sun photometer measurements (see Fig. 5.3) shows a dominant fine mode, but there is also a significant amount of coarse-mode particles. Microphysical aerosol properties retrieved from the radiometric measurements are listed in Fig. 5.4 and show also typical values for a dominating fine mode. The total AOT of 1.05 is mainly caused by the fine-mode AOT with a value of 1.0. The coarse-mode AOT with a value of 0.05 is not as high as the size distribution might suggest. According to the quicklook in Fig. 5.4 and an effective radius of 2.7 μm for the coarse mode, it can be assumed that the amount of coarse-mode particles is due to unscreened cirrus clouds. The Ångström exponent of 0.9 indicates a strong wavelength dependence of the AOT which is typical for fine-mode events.

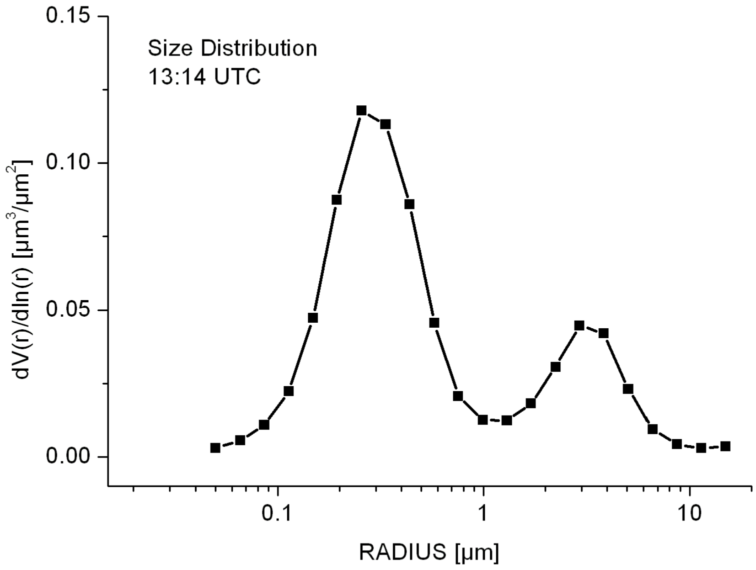

Figure 5.3: Size distribution obtained from the AERONET observation at 13:14 UTC on 6 April 2009.

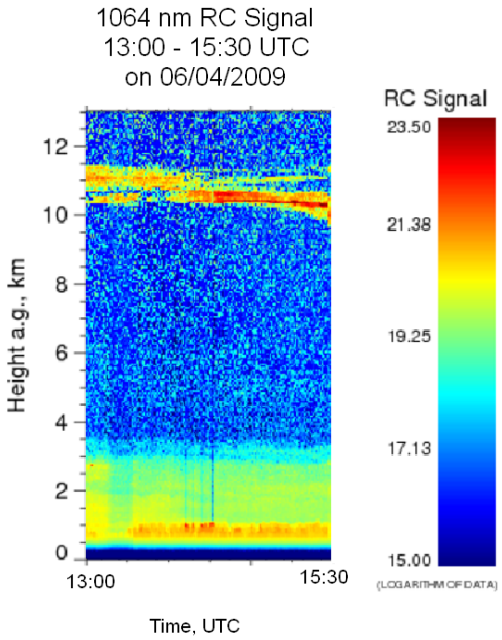

Total AOT	1.05
Fine-mode AOT	1.01
Coarse-mode AOT	0.04
$\mathring{a}_t$	0.9
$\mathring{a}_f$	0.9
$\mathring{a}_c$	0.08
V_t	0.208 $\mu m^3/\mu m^2$
V_f	0.154 $\mu m^3/\mu m^2$
V_c	0.054 $\mu m^3/\mu m^2$
$r_{eff,f}$	0.24 μm
$r_{eff,c}$	2.7 μm

Figure 5.4: Left: Range-corrected signal at 1064 nm between 13:00 and 15:30 UTC on 6 April 2009. Vertical resolution is 60 m and time resolution is 30 s. Right: Aerosol properties derived from the AERONET observations.

To investigate the source of the aerosol three backward trajectories for the observation heights of 1000, 2000, and 3000 m were calculated with HYSPLIT (see Fig. 5.5). The red trajectory follows the air flow caused by the high pressure system over North Germany and Poland. The air parcels traveled in atmospheric layers below 1000 m. Therefore, it is most likely that the fine particles are caused by industrial pollution over Central Europe. Another source of fine particles may be fires which occur from time to time over East Europe. The MODIS Firemap reveals several fires in the week before the observation in the eastern Ukraine and in Hungary (see Fig. 5.6). Thus combustion particles could also contribute to the fine mode.

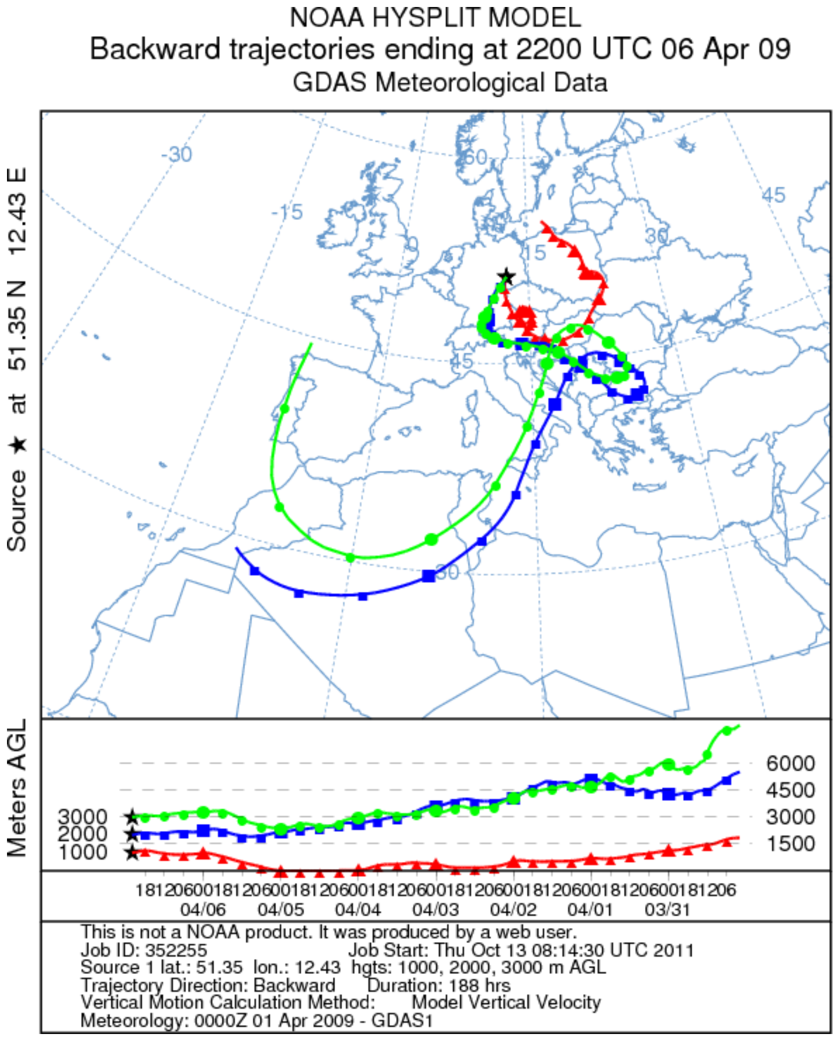

Figure 5.5: Backward trajectories simulated with HYSPLIT for the arrival at Leipzig at 22 UTC on 6 April 2009 and for the observation heights 1000 m (red), 2000 m (blue), and 3000 m (green).

The other two trajectories for observation heights of 2000 and 3000 m show a similar transport pattern. They would suggest that the coarse-mode particles could be Saharan dust, although the travel height was above 4500 m over the Sahara region. Therefore, DREAM and FLEXPART calculations were carried out (see Fig. 5.7 and 5.8). The FLEXPART output shows for the layers from 0.5 to 1 km and 1 to 3 km a high residence time over East Europe, what is expected for aerosol particles that followed the red trajectory. There is also a probability for residence over the Saharan desert, but the DREAM calculation does not indicate any dust loading over Germany at the observation time. This leads to the conclusion that the coarse mode was not caused by dust particles. They can be rather attributed to the cirrus clouds.

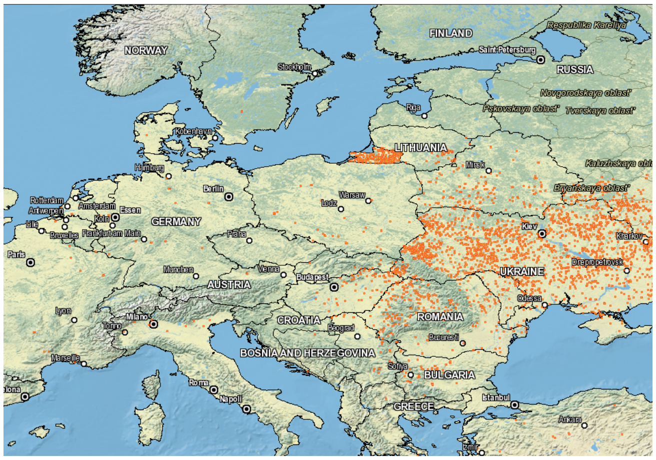

Figure 5.6: MODIS Firemap of all fires observed between 31 March and 6 April 2009.

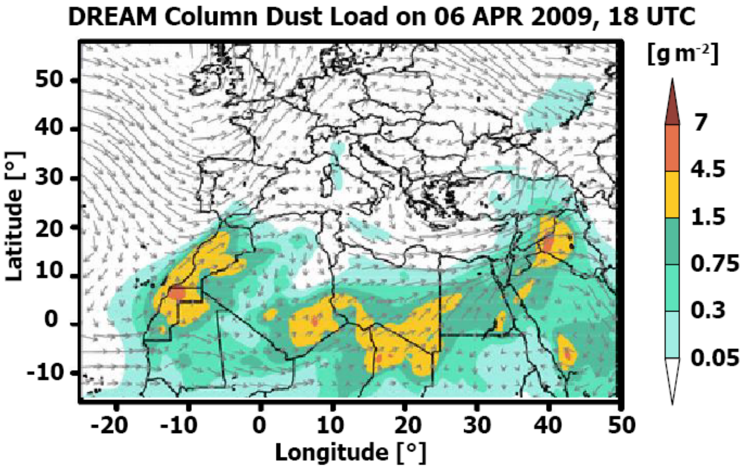

Figure 5.7: DREAM dust forecast at 18 UTC on 6 April 2009.

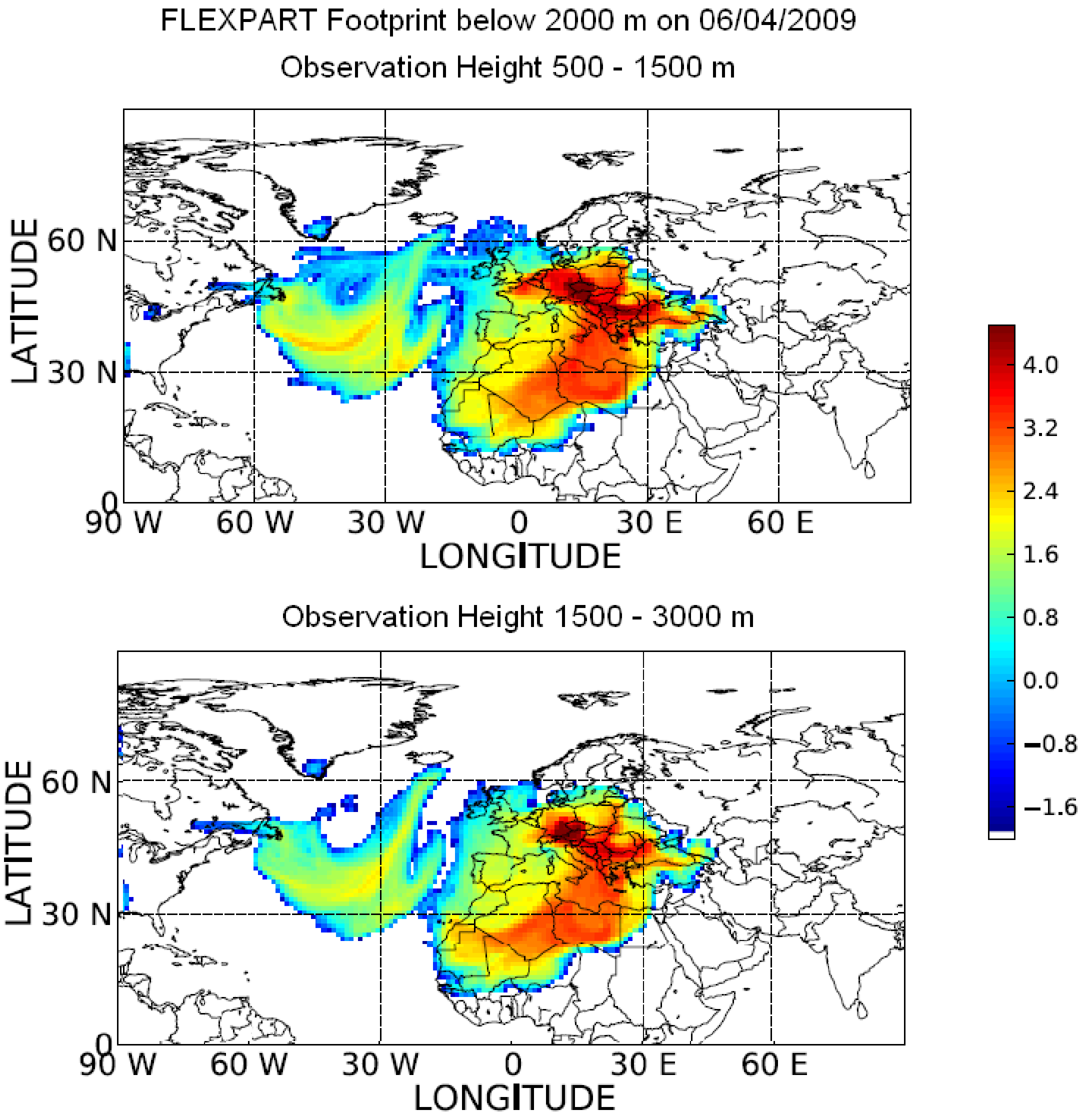

Figure 5.8: FLEXPART simulations for the integrated residence time of the particles that traveled below 2000 m within the last 10 days until the observation on 6 April 2009 for observation heights in 500–1500 m (upper plot) and in 1500–3000 m (lower plot). The colors represent the logarithm of the integrated residence time in a grid box in seconds for 10-day integration time.

5.1.2 Retrieved optical and microphysical properties

The raw lidar data were overlap-corrected and constant volume concentrations were assumed below 1020 m. Thus the concentration profiles were calculated for the range between that height and the reference point at 9 km. Fig. 5.9 shows the results for the evening measurement between 19:38 and 21:33 UTC. Backscatter and extinction coefficients are recalculated from the concentration profiles according to Eq. (3.31) and (3.32). The values are quite large which is in accordance with the observed AOT. There is a clear wavelength dependenc as one would expect for a fine-mode event. The lidar ratio fluctuates around 75 sr and thus confirms the previously discussed aerosol types which originate from combustion and industrial pollution (see Section 2.4). Above the aerosol layer the lidar ratio is constant at 35 sr and indicates clean conditions.

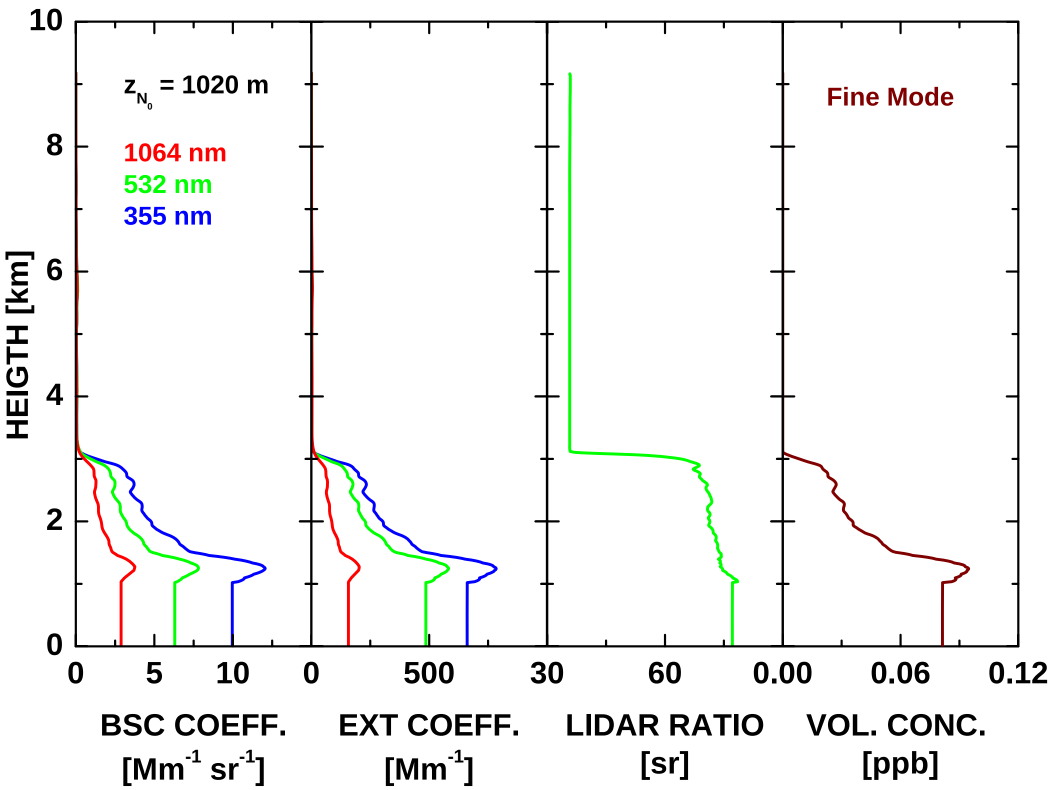

Figure 5.9: Optical and microphysical properties between 19:38 and 21:33 UTC on 6 April 2009, for calculations with $z_{N_0} = 1020$ m and the reference point at 9 km. The different colors indicate the different wavelengths (355 nm: blue, 532 nm: green, 1064 nm: red). Only the fine-mode concentration is shown.

Only the profile of the fine-mode concentration is shown, because the cirrus contamination in the radiometric measurements would not lead to a reasonable coarse-mode profile. The unity of ppb corresponds to $\mu\text{m}^{-3}/\text{cm}^{-3}$ such that 0.1 ppb = 100 $\mu\text{m}^{-3}/\text{cm}^{-3}$. The fine-mode concentration increases from 3 km downwards to 1.2 km. It then decreases somewhat and is finally set constant at height z_{N_0} down to the ground. The shape of the fine-mode profile also fits the range-corrected signal in the quicklook.

Finally, the recalculated backscatter coefficient at 532 nm is compared to the backscatter profile derived after the Raman method (see Fig. 5.10). Tab. **??** gives values of the backscatter and extinction coefficients and of the lidar ratio for selected heights. The profiles agree very well in the range between 1.5 and 3 km. Above 3 km, there are only small deviations which are within the error margins of the different methods. Around 1.5 km there is a difference of about 2 $\mathrm{Mm^{-1}sr^{-1}}$ between the Raman profile and the calculated one. It is most likely that this discrepancy is due to uncertainties in the retrieval code as the Raman method is very accurate, because there is no need for an overlap correction. It was already discussed that the radiometric data were influenced by cirrus clouds. The recalculated backscatter coefficient is dependent on both fine-mode and coarse-mode concentration. By assuming too much coarse-mode particles, the backscatter coefficient would be underestimated as b_f is larger than b_c in this case. Other sources for errors are the calculations of the molecular profiles and the overlap effect. Especially this case is sensitive to the overlap effect, because most of the aerosol is confined to the overlap-influenced range.

Table 5.1: Backscatter and extinction coefficients as well as lidar ratios in different heights derived with the retrieval algorithm and the Raman method, respectively, between 19:38 and 21:33 UTC on 6 April 2009.

	Combined retrieval			Raman method		
Height	β [$\mathrm{Mm^{-1}sr^{-1}}$]	α [$\mathrm{Mm^{-1}}$]	S [sr]	β [$\mathrm{Mm^{-1}sr^{-1}}$]	α [$\mathrm{Mm^{-1}}$]	S [sr]
1 km	6.3	486	77	7.3	–	–
1.5 km	4.9	364	74	6.7	466	69
2 km	3.2	229	71	3.4	230	69
2.5 km	2.4	168	71	2.5	153	61
3 km	0.9	60	64	2.1	108	50

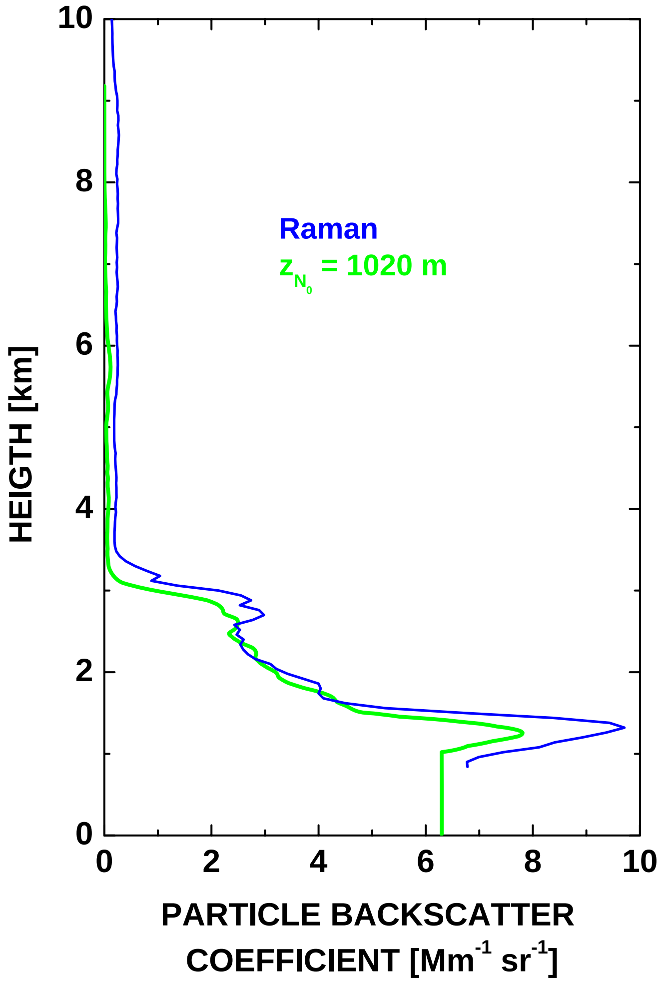

Figure 5.10: Comparison of the backscatter profiles at 532 nm, derived using the retrieval algorithm (green) and the Raman method (blue) between 19:38 and 21:33 UTC on 6 April 2009.

5.2 Case of 30 May 2008

5.2.1 Meteorological situation and database

During May 2008 a strong Saharan dust outbreak towards Central Europe was observed. A low-pressure system with multiple centers was located over Europe (see Fig. 5.11). A southerly to south-easterly flow towards Leipzig prevailed. A deep aerosol layer occurred over Leipzig at the end of the month. Photometer measurements showed an AOT of 0.4 at 500 nm and higher. Lidar measurements were performed from 28 to 30 May 2008. According to accompanying radiometric measurements, the time period from 09:10 to 10:31 UTC on 30 May 2008 was chosen as a favorable observational period.

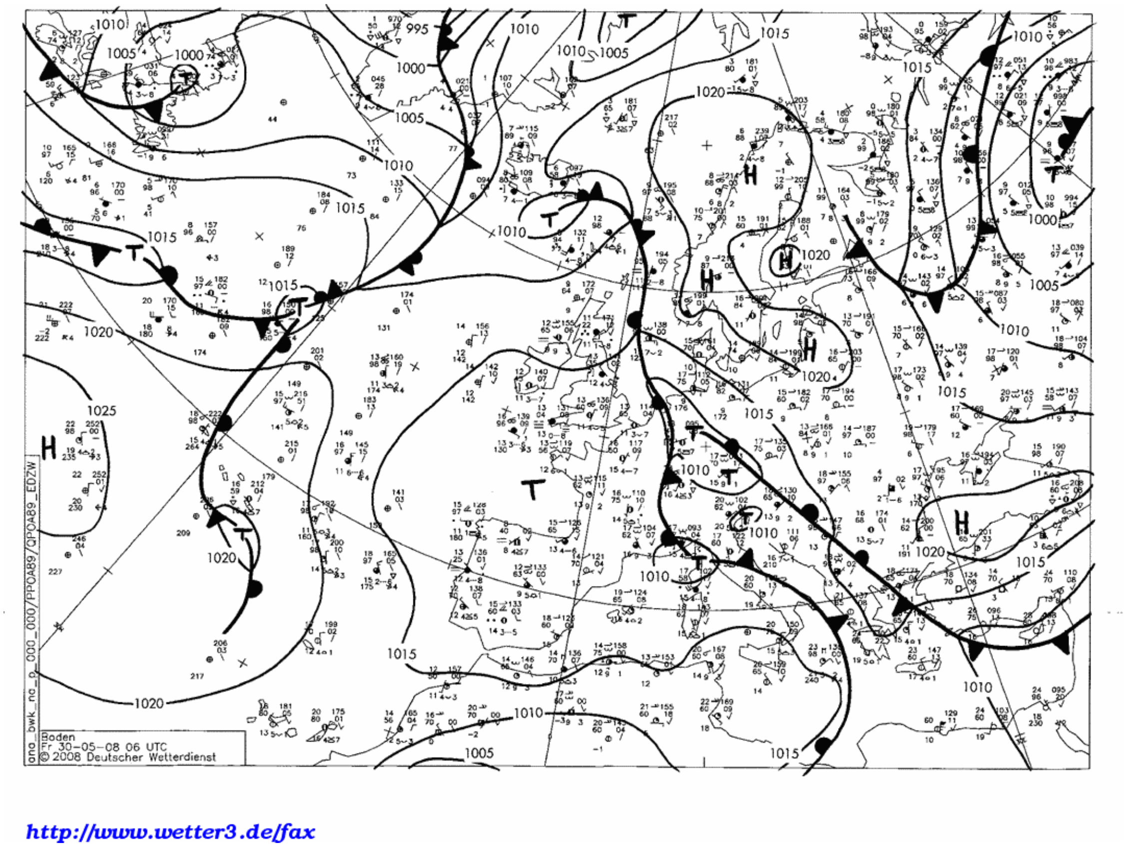

Figure 5.11: DWD-analysis weather chart for the ground level at 6 UTC on 30 May 2008.

Fig. 5.12 gives an overview about the aerosol situation between 09:10 and 10:31 UTC on 30 May 2008. Up to a height of 5.5 km a Saharan dust layer was present. The microphysical characteristics retrieved from sun photometer measurements suggest a coarse-mode event (compare Tab. 5.1), in particular the size distribution shows a dominant coarse mode. The Ångström exponent of 0.41 indicates a weak wavelength dependence of the AOT which is typical for bigger particles. The coarse-mode AOT with a value of 0.29 was more than twice as high as the fine-mode AOT.

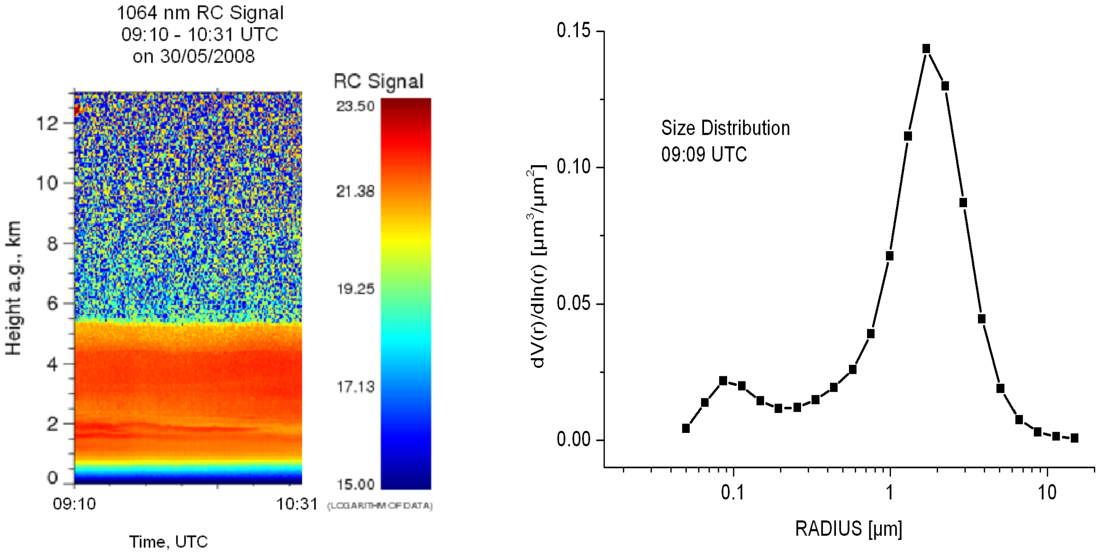

Figure 5.12: Left: Range-corrected signal at 1064 nm between 09:10 and 10:31 UTC on 30 May 2008. The vertical resolution is 60 m, the temporal resolution is 30 s. Right: Size distribution at 09:09 UTC derived from the AERONET observations.

Table 5.2: Optical and microphysical aerosol properties obtained from radiometric measurements around 13:14 UTC on 6 April 2009.

Total AOT	0.43
Fine-mode AOT	0.14
Coarse-mode AOT	0.29
$\mathring{a}_t$	0.48
$\mathring{a}_f$	1.87
$\mathring{a}_c$	0.22
V_t	0.221 $\mu\mathrm{m}^3/\mu\mathrm{m}^2$
V_f	0.033 $\mu\mathrm{m}^3/\mu\mathrm{m}^2$
V_c	0.188 $\mu\mathrm{m}^3/\mu\mathrm{m}^2$
$r_{eff,f}$	0.12 μm
$r_{eff,c}$	1.5 μm

Simulation results for the determination of the aerosol source region are shown in Fig. 5.13. HYSPLIT calculations were done for arrival heights of 2000, 3000, and 4000 m. The origin of all three trajectories was in North Africa. The air mass traveled six days before reaching Central Europe. The Saharan dust layer spent several days over Southern Europe, so that mixing with marine and urban aerosol was possible in the lower parts of the dust layer. According to FLEXPART-calculations in Fig. 5.14 the residence time over parts of south-eastern Europe was even higher than over the Saharan desert. The MODIS Firemap (see Fig. 5.15) shows that a contribution of combustion can be ruled out. Fig. 5.16 finally presents the DREAM results and clearly shows that the Saharan dust outbreak influenced large parts of Europe on 30 May 2008.

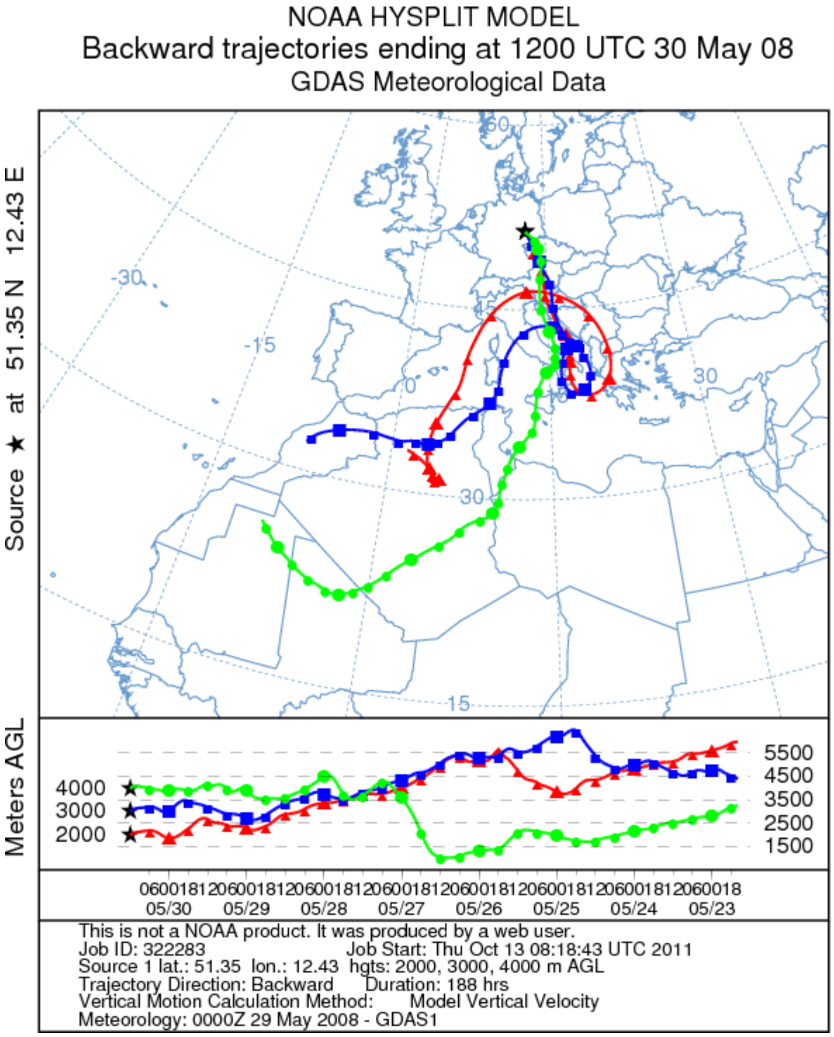

This is not a NOAA product. It was produced by a web user.
Job ID: 322283 Job Start: Thu Oct 13 08:18:43 UTC 2011
Source 1 lat.: 51.35 lon.: 12.43 hgts: 2000, 3000, 4000 m AGL
Trajectory Direction: Backward Duration: 188 hrs
Vertical Motion Calculation Method: Model Vertical Velocity
Meteorology: 0000Z 29 May 2008 - GDAS1

Figure 5.13: Backward trajectories simulated with HYSPLIT for the arrival at Leipzig at 12 UTC on 30 May 2008 and for the observations heights 2000 m (red), 3000 m (blue), and 4000 m (green).

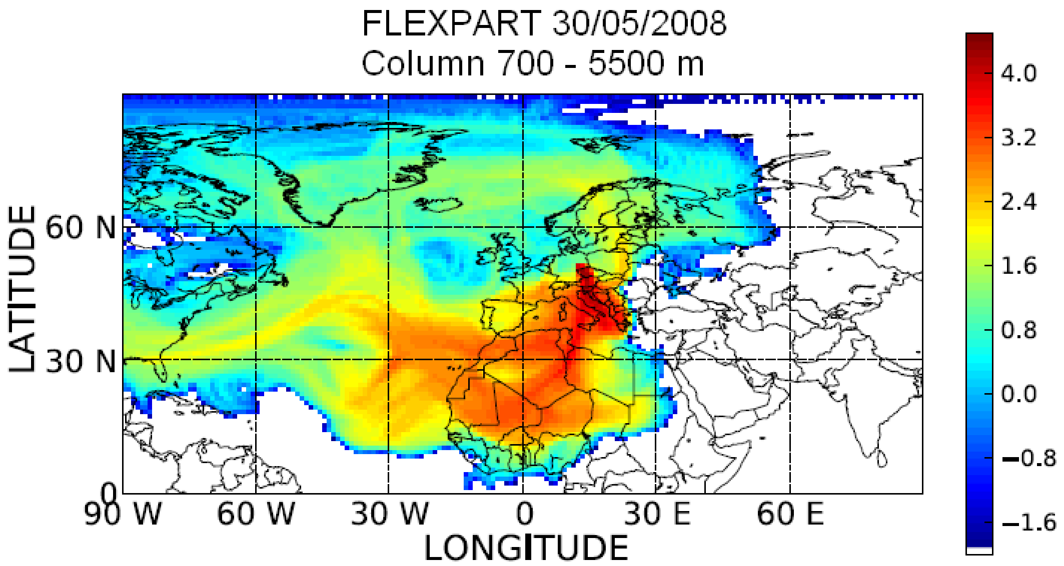

Figure 5.14: FLEXPART simulations for the integrated residence time of the particles within the last 10 days until the observation on 30 May 2008 for the layer between 700 and 5500 m. The colors represent the logarithm of the integrated residence time in a grid box in seconds for 10-day integration time.

Figure 5.15: MODIS Firemap with all fires observed between 23 and 30 May 2008.

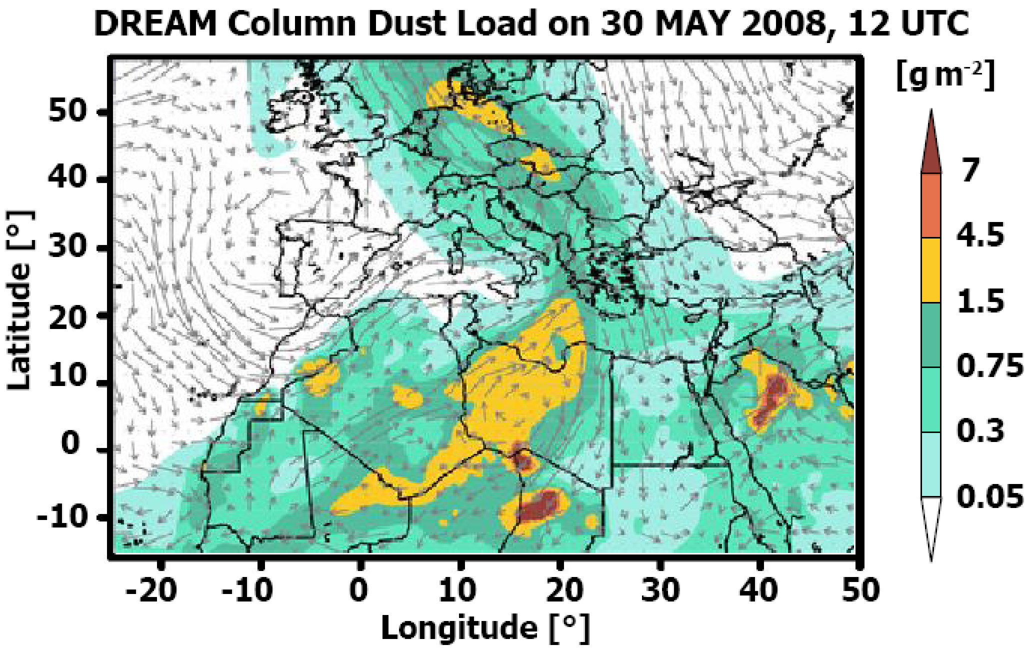

Figure 5.16: DREAM dust forecast at 12 UTC on 30 May 2008.

5.2.2 Retrieved optical and microphysical properties

The raw lidar data were overlap-corrected as described in Section 4.1. The calculations were run for constant concentrations between ground and 600 m and between ground and 1200 m. Profiles of optical and microphysical profiles were retrieved for the range between these heights and a reference point at 10.5 km. Fig. 5.17 shows the calculation results. The differences in the results are small, i.e. the influence of the selected height z_{N_0} is small in this case. Significant differences occur only in the range below z_{N_0}. The backscatter and extinction coefficients are nearly wavelength-independent. In accordance, the volume concentration profiles show a dominant coarse mode in the range between ground and 6 km. The fine-mode contribution is almost negligible. For both cases the lidar ratio is in the range between 50 and 55 sr which is a typical for Saharan dust (*Tesche et al.*, 2009b). Additionally, the Ångström exponent was calculated from the extinction profiles at 355 and 532 nm. For the dust layer, $\mathring{a}$ is smaller than 0.5 and thus indicates coarse-mode particles.

Whereas the retrieval results are in good agreement with the quicklook below 6 km, there is obviously an overestimation of the particle amount above the dust layer. This overestimation pertains to both modes. A possible explanation is that the fine-mode particles are concentrated below z_{N_0} and the respective spectral signature is thus contained only in the sun photometer data, but not in the lidar signals. Probably the algorithm distributes the extant information content over the entire range of the profiles, which might in turn affect the coarse-mode results.

Another problem refers to the recalculated backscatter coefficient. Above 2 km it shows smaller values for 355 nm than for 532 and 1064 nm. For strong coarse-mode events like the Saharan dust outbreak this is not unlikely. However, the reasons for the spectral order of the backscatter coefficients are unclear, and may be related to the assumptions of the extinction-to-backscatter ratio in the retrieval code for the radiometric properties. In particular for non-spherical particles the reproducibility of the lidar ratio is difficult.

The backscatter and extinction profiles are recalculated from the concentration profiles together with radiometric information (see Eq. (3.31) and (3.32)). Corresponding values of backscatter and extinction coefficients for fine and coarse mode which are retrieved from the sun photometer measurements are listed in Tab. 5.2. It reveals the following relation:

$$\begin{gathered}
b_f(355\text{ nm}) > b_f(532\text{ nm}) > b_f(1064\text{ nm}) \\
b_c(355\text{ nm}) < b_c(532\text{ nm}) < b_c(1064\text{ nm}) \\
a_f(355\text{ nm}) > a_f(532\text{ nm}) > a_f(1064\text{ nm}) \\
a_c(355\text{ nm}) < a_c(532\text{ nm}) < a_c(1064\text{ nm}).
\end{gathered}$$

Table 5.3: Values of the backscatter and extinction coefficient b and a retrieved from radiometric measurements at 9 UTC on 30 May 2008. They are listed for the three wavelengths 355, 532, and 1064 nm as well as for the two aerosol modes.

λ	b_f [km^{-1}sr^{-1}]	b_c [km^{-1}sr^{-1}]	a_f [km^{-1}]	a_c [km^{-1}]
355 nm	$1.54 * 10^{-4}$	$1.51 * 10^{-5}$	$9.66 * 10^{-3}$	$1.09 * 10^{-3}$
532 nm	$1.08 * 10^{-4}$	$2.41 * 10^{-5}$	$6.21 * 10^{-3}$	$1.13 * 10^{-3}$
1064 nm	$4.04 * 10^{-5}$	$3.15 * 10^{-5}$	$2.47 * 10^{-3}$	$1.34 * 10^{-3}$

Even though some uncertainties remain regarding the backscatter coefficients, there is consistency and good agreement between the different derived properties. Especially for Saharan dust with its large non-spherical particles the retrieval of optical and microphysical properties is complex and some questions are still unsolved (*Müller et al.*, 2010a,b). Further studies have to be done, but for this work the chosen case already leads to good results.

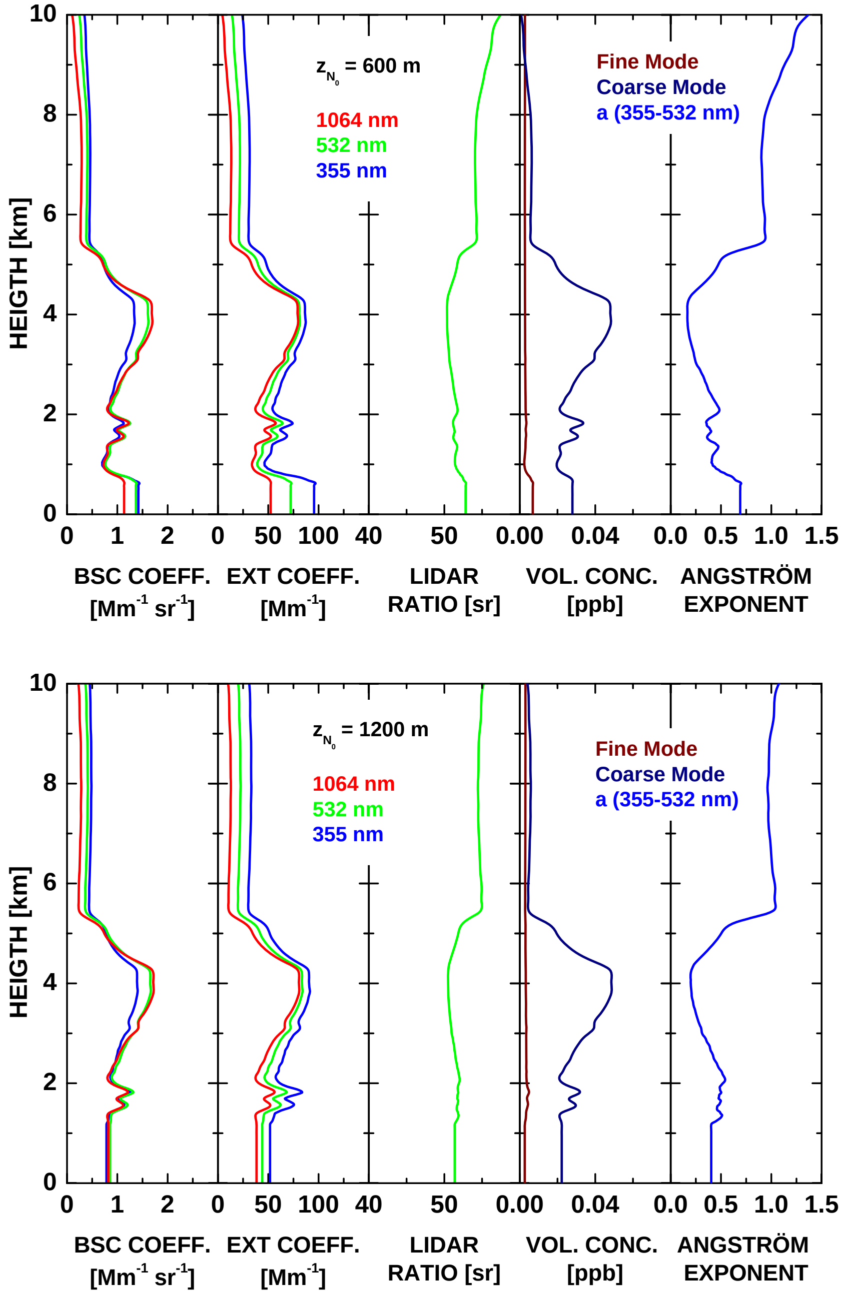

Figure 5.17: Profiles of the backscatter and the extinction coefficients as well as the lidar ratio and the two aerosol mode concentrations between 09:10 and 10:31 UTC on 30 May 2008. Additionally the Ångström exponent at 355–532 nm is given. The upper plot shows results for a constant concentration between ground and 600 m. The lower profiles were calculated for constant concentrations up to 1200 m. The height of the reference point is 10.5 km. The different colors indicate the different wavelengths (355 nm: blue, 532 nm: green, 1064 nm: red) and the two concentration modes (fine: dark red, coarse: dark blue).

Finally, Fig. 5.18 shows a comparison of the backscatter profiles at 532 nm for the two different z_{N_0}, together with a backscatter profile retrieved after the Klett method. In the range between 2 and 5 km, there is good agreement between the recalculated algorithm profiles and the Klett profiles as also the values listed in Tab. **??** show. The recalculated profiles almost match each other, significant deviations only occur below 1.5 km. Differences to the Klett profile increase towards the ground which can be due to the assumption of a constant lidar ratio in the calculations. For the shown profile it was assumed to be 50 sr which is close to the values retrieved with the algorithm. Calculations of the Klett profile start around the reference point and go downwards to the ground, thus already small deviations can lead to significant differences as the errors would sum up. However, the underestimation of the backscatter coefficients in the near range by the retrieval algorithm can also be explained by the overestimation above 5 km, where the differences between recalculated profiles and Klett profiles are quite large. The assumption of z_{N_0} lead to a fixed particle concentration below z_{N_0}. If this amount is underestimated, somewhere else an overestimation appears.

Table 5.4: Comparison of the backscatter coefficients in selected heights, derived with the retrieval algorithm for $z_{N_0} = 600$ m and $z_{N_0} = 1200$ m and with the Klett method on 30 May 2008, 09:10–10:31 UTC.

	β [Mm^{-1}sr^{-1}]		
Height	$z_{N_0} = 600$ m	$z_{N_0} = 1200$ m	Klett
1 km	0.76	0.86	1.1
2 km	0.93	0.96	0.62
3 km	1.3	1.3	1.1
4 km	1.6	1.7	1.7
5 km	0.77	0.81	1.0

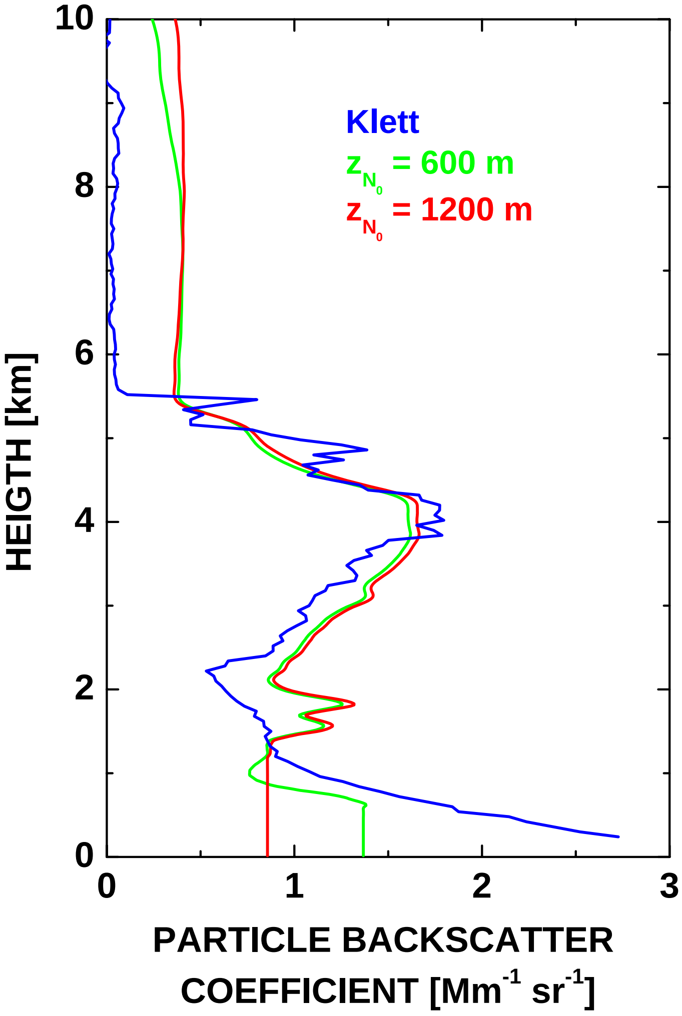

Figure 5.18: Comparison of the particle backscatter coefficients for $z_{N_0} = 600$ m (green) and $z_{N_0} = 1200$ m (red), together with a Klett profile (blue) between 09:10 and 10:31 UTC on 30 May 2008.

5.3 Error estimation

For the cases discussed in Section 5.1 and 5.2 different profiles of fine-mode and coarse-mode concentrations were obtained dependent on the selected depth of the range for constant concentrations and the selected reference height. The profiles were used to estimate the error margin of the altitude distributions. According to the dominating mode the fine-mode profiles of 6 April 2009 and the coarse-mode profiles of 30 May 2008 were chosen to quantify the uncertainties of the fine-mode and the coarse-mode calculations, respectively. Fig. 5.19 show mean profiles of the altitude distributions of both modes together with the standard deviation. In addition, Tab. 5.3 lists the relative error for selected layers. It gives a more detailed specification of the error margins.

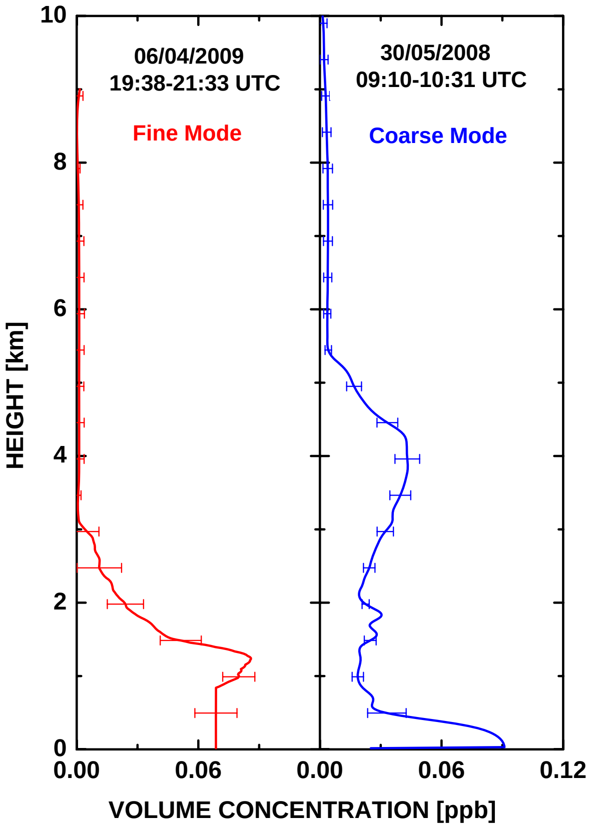

Figure 5.19: Profiles of mean fine-mode (red) and coarse-mode (blue) concentrations with the respective error bars which represent the standard deviation. The error estimation for the fine mode is based on 6 April 2009 and for the coarse mode on 30 May 2008.

Table 5.5: Relative errors for different layers of the fine-mode and coarse-mode concentration profiles based on several calculations for 6 April 2009 and 30 May 2008, respectively.

Layer	Fine mode [%]	Coarse mode [%]
0 – 0.5 km	15	70
0.5 – 1 km	13.5	10
1 – 1.5 km	12	12
1.5 – 2 km	29	9
2 – 2.5 km	65	11
2.5 – 3 km	100	12
3 – 4 km	-	13
4 – 5 km	-	16

The fine-mode uncertainty fluctuates around 13% below 1.5 km and increases then to 30% to 65% for the range between 1.5 and 3 km. The error for the coarse mode is smaller with values of 9% to 16%, only below 0.5 km the uncertainty is quite large with 70%. This demonstrates the influence of the overlap effect, but as already discussed before it does not affect the distribution in higher atmospheric layers in this case.

Furthermore, the larger the optical thickness of the aerosol layer is, the less are the errors. The range of less reliable data has a smaller influence on an aerosol layer that reaches up to 5 or 6 km than on an aerosol layer that is confined to the planetary boundary layer. Thus the smallest relative errors occur for the Saharan dust event. For the case of the Eyjafjallajökull eruption discussed in the next section, the relative error is estimated to 25% for the fine-mode concentration and to 10% for the coarse mode.

For further studies, the height of z_{N_0} has to be determined for each case individually. The reference point should be around 9 or 10 km. The evaluation of cases with high AOT is more promising than of situations where the aerosol is mainly confined to the overlap-influenced range. In order to reduce the uncertainty additional near-range measurements should be provided for such cases if possible.

5.4 Case of 19 April 2010

The volcanic eruption of the Eyjafjallajökull on 14 April 2010 provides an opportunity to examine the approach for the distinction of aerosol types and to determine fine-mode and coarse-mode concentrations. During a first phase from 14 to 17 April 2010 several eruptions took place. Within one to two days the ash cloud was transported to Europe. Thus already on 16 April 2010 high values of the AOT were observed at Leipzig. The ash cloud was then blown away westwards due to a high-pressure system that reached from the North Atlantic to Central Europe. With a westerly flow it returned to Germany on 19 and 20 April 2010. All the time, there was also a constant northerly air flow over the Norwegian Sea. Thus HYSPLIT calculations (see Fig. **??**) show that only particles observed in a height around 4200 m followed the flow caused by the high pressure. According to HYSPLIT aerosol particles located between 700 and 2000 m were transported to Leipzig with a northwesterly flow.

The volcanic aerosol observed on 19 April 2010 was already aged (4 to 5 days old) and consisted of ash particles and a significant amount of fine particles. In particular, the fine mode can be caused by sulfate particles which originated from sulfur dioxide that was released during the eruption. The focus in this section lies on the determination of the particle mass concentration. Its calculation is explained in Section 5.4.2 which is in accordance with the calculations provided in the paper by *Ansmann et al.* (2011). In Section 5.4.3 the obtained results are compared to the ones in the mentioned paper.

5.4.1 Database of 19 April 2010

The analysis is based on the data of 19 April 2010 since the most extensive aerosol layer was observed on this day. Sun photometer and lidar measurements were carried out the whole day. Hourly backscatter profiles were calculated for 532 nm. A strong aerosol layer occured up to 2.5 km (see Fig. 5.20). Between 4 and 5 km a second layer was found. Around 13 UTC a new layer between 1 and 2 km appeared, indicating advection of the aged ash from the west. In the case study, the photometer measurement at 14:49 UTC was considered. In the afternoon around 15:15 UTC some clouds appeared. Thus lidar data were averaged over the period from 14:01 to 15:12 UTC in order to assure cloud-free conditions.

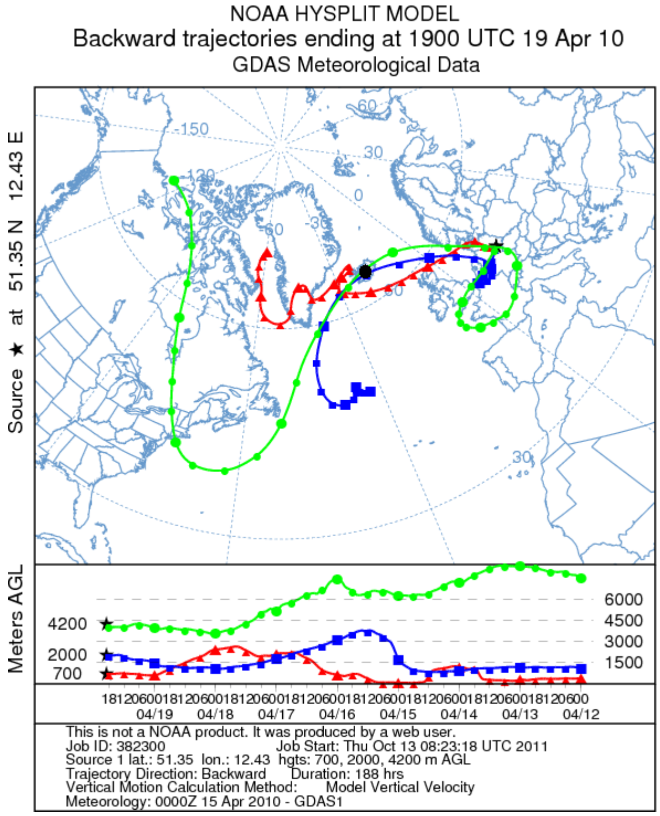

Figure 5.20: Backward trajectories simulated with HYSPLIT for the arrival at Leipzig at 19 UTC on 19 April 2010 and for the observation heights 700 m (red), 2000 m (blue), and 4200 m (green). The black point indicates the location of the volcano.

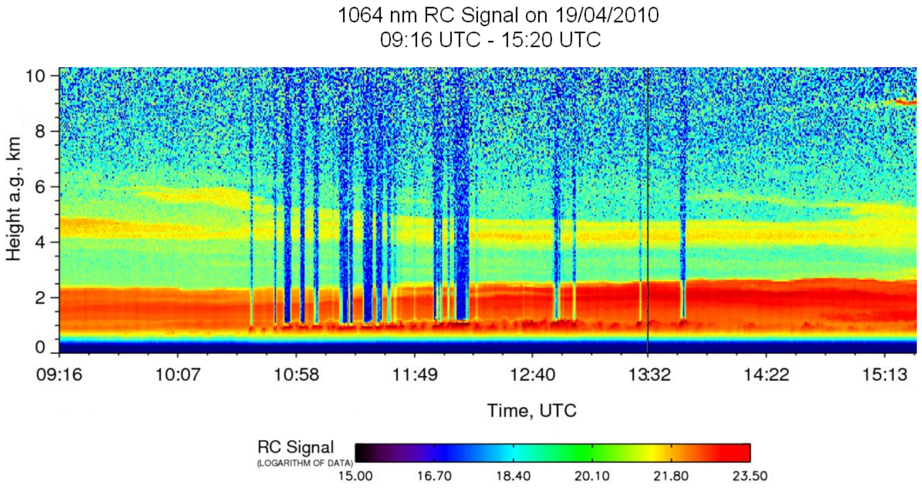

Figure 5.21: Range-corrected signal at 1064 nm on 19 April 2010, 09:16–15:20 UTC, with a spatial resolution of 60 m and a time resolution of 30 s.

Table 5.6: Optical and microphysical aerosol properties obtained from radiometric measurements around 15 UTC on 19 April 2010.

Total AOT	0.65
Fine-mode AOT	0.49
Coarse-mode AOT	0.16
$\mathring{a}_t$	1.09
$\mathring{a}_f$	1.48
$\mathring{a}_c$	0.24
V_t	0.158 μm^3/μm^2
V_f	0.08 μm^3/μm^2
V_c	0.078 μm^3/μm^2
$r_{eff,f}$	0.18 μm
$r_{eff,c}$	1.4 μm

The raw lidar data were overlap-corrected and constant concentrations were assumed up to 550 m. The profiles were retrieved between 550 m and the reference height of 9 km. Results are shown in Fig. 5.21. The backscatter profiles differ from each other in the range between 1 and 2 km and are quite similar to each other above 2 km. Thus they indicate fine-mode particles below 2 km and coarse-mode particles between 2 and 3 km. There is a second peak apparent between 4 and 5 km, also indicating coarse-mode particles. The profiles of the extinction coefficients show a similar shape. The lidar ratio ranges from 60 to 80 sr with two distinct minima at 2.5 km and 4.5 km. That fits to the values given in *Ansmann et al.* (2011) as the lidar ratio of ash varies between 40 and 60 sr and of non-ash particles between 40 and 80 sr.

According to the backscatter profiles, a fine-mode layer is apparent at heights below 3 km. The layer of coarse-mode particle reaches from 1 to 3 km with a distinct peak at 2 km. Around 4.5 km there is a second layer of coarse-mode particles. The underlying colored areas indicate the error margins of fine-mode and coarse-mode concentrations. According to Section 5.3 the error for the fine mode was chosen to be 25% and for the coarse mode 10%. Volcanic ash usually consists of coarse particles, while the sulfate particles have much smaller sizes. Thus the coarse-mode profile can be used to represent the ash and the fine-mode profile to describe the sulfate.

An additional calculation was performed, because the backscatter and extinction coefficients decreased to almost zero in the near range. Assuming a well-mixed boundary layer it seems to make more sense having a backscatter coefficient at 532 nm of about

3 $\mathrm{Mm}^{-1}\mathrm{sr}^{-1}$ and a corresponding extinction coefficient of about 200 Mm^{-1}. Therefore, the second calculation was run with $z_{N_0} = 1020$ m and the results are shown in Fig. 5.22. As expected deviations to the previous calculation occur in the range below 1000 m. Also, the maximum values around 2 km are somewhat smaller. The lidar ratio did also change significantly. It is around 80 sr up to 2 km and decreases then to 45 sr for the range above 3 km. Thus the lidar ratio for the upper ash layer is smaller than before and it does not show an increase between the ash layers in the height range between 3 and 4 km.

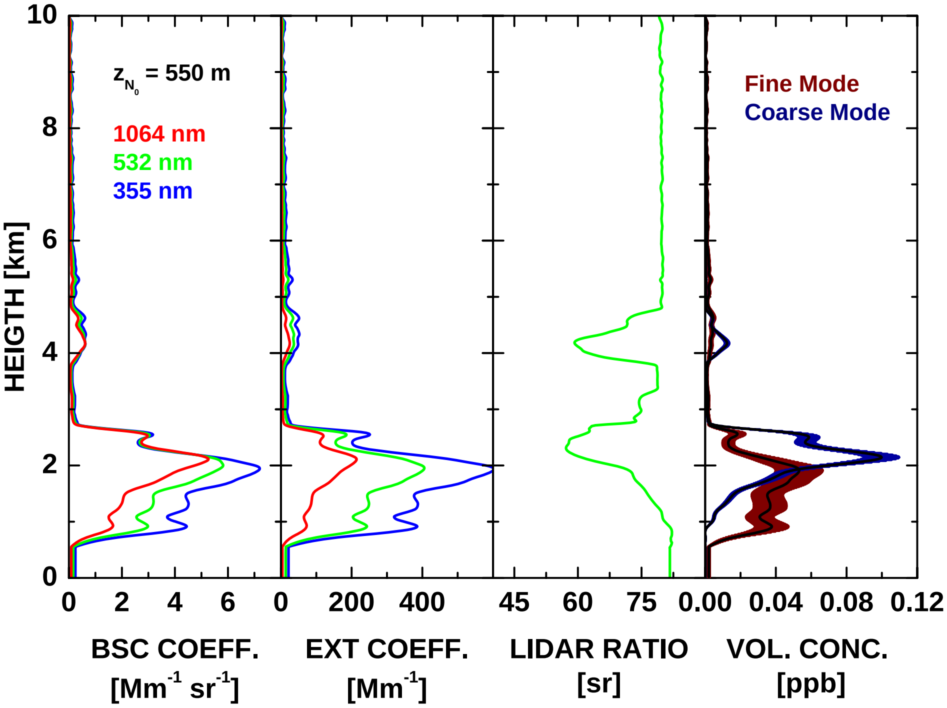

Figure 5.22: Optical and microphysical properties between 14:01 and 15:12 UTC on 19 April 2010 with $z_{N_0} = 550$ m and a reference point at 9 km. The different colors indicate the different wavelengths (355 nm: blue, 532 nm: green, 1064 nm: red) and the two concentration modes (fine: dark red, coarse: dark blue).

The radiometric retrievals show that the volume fractions of ash and sulfate particles are almost equal (see Tab. 5.4), but the contribution to the AOT comes mainly from the fine mode. The Ångström exponent also indicates a mixed aerosol as the value is too large for volcanic ash and too small for an aerosol consisting only of fine particles.

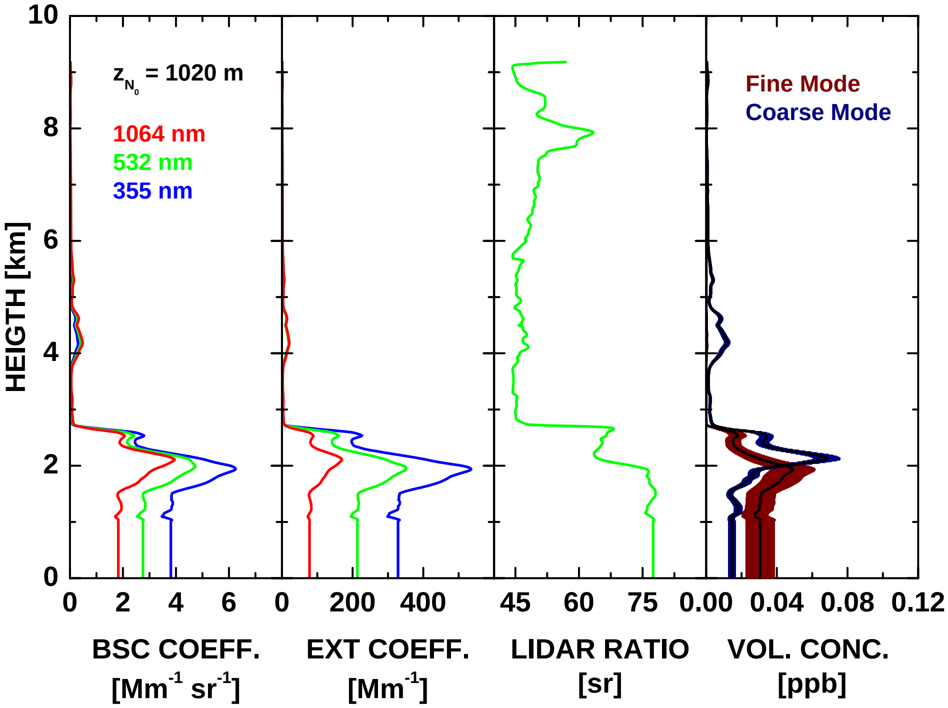

Figure 5.23: Optical and microphysical properties between 14:01 and 15:12 UTC on 19 April 2010 with $z_{N_0} = 1020$ m and a reference point at 9 km. The different colors indicate the different wavelengths (355 nm: blue, 532 nm: green, 1064 nm: red) and the two concentration modes (fine: dark red, coarse: dark blue).

5.4.2 Calculation of the particle mass concentration

To quantify the amount of aerosol particles the particle mass concentration can be calculated. According to *Ansmann et al.* (2011) the following equations are used to calculate the mass concentrations m_c and m_f of ash and non-ash particles, respectively:

$$m_c = \rho_c(\overline{V_c/AOT_c})\beta_c S_c, \tag{5.1}$$

$$m_f = \rho_f(\overline{V_f/AOT_f})\beta_f S_f. \tag{5.2}$$

ρ_c and ρ_f are the mass densities of the ash and non-ash. They are assumed to be 2.6 ± 0.6 g/cm^3 and 1.5 ± 0.3 g/cm^3, respectively. $\overline{V_{f,c}/AOT_{f,c}}$ are so-called volume-to-AOT conversion factors which can be retrieved from the sun photometer measurements. The AERONET observations revealed a mean ash conversion factor of 0.605 ($\pm$ 0.1) $\times 10^{-6}$ m and a mean non-ash conversion factor of 0.177 ($\pm$ 0.016) $\times 10^{-6}$ m. More details about their calculation can be found in *Ansmann et al.* (2011). It is assumed that both components are mixed externally and correspond to coarse and fine mode, respectively. S_c and S_f are the lidar ratios which vary between 40 and 80 sr for non-ash or fine particles, whereas the lidar ratio for ash is set constant to 50 sr. β_c and β_f are the backscatter coefficients that were caused by ash and fine-mode aerosol. *Ansmann et al.* (2011) separated them by using depolarization ratios after a method described in *Tesche et al.* (2009a). Depolarization ratios of 35% to 40% indicate ash (*Ansmann et al.*, 2010), while non-ash particles are assumed to have depolarization ratios below 5%. In this work, backscatter coefficients were calculated from the two concentration profiles with corresponding integral values from radiometric measurements:

$$\begin{aligned} \beta_c(z) &= b_c(z) C_c(z), \\ \beta_f(z) &= b_f(z) C_f(z). \end{aligned} \tag{5.3}$$

5.4.3 Comparison with the depolarization method

Fig. 5.23 shows the particle mass concentrations for the ash and the fine-mode fraction. The results of the combined retrieval for different z_{N_0} are compared to the results retrieved by the depolarization method. The lidar ratios were varied to demonstrate the influence. *Ansmann et al.* (2011) used a lidar ratio of 50 sr for ash and 60 sr for non-ash particles, whereas the combined retrieval results suggested a lidar ratio of 60 sr for ash and 80 sr for the fine fraction.

For $z_{N_0} = 550$ m the curves show good agreement, especially for the ash mass concentration. However, by using the combined retrieval method the ash layer around 5 km is not as extensive as the one determined with the depolarization method. Furthermore, the retrieval algorithm for combined lidar and sun photometer data does not calculate as much non-ash particles as the depolarization retrieval. Even by taking the error range into account, there is still a significant deviation between 0.5 and 1.5 km. With larger lidar ratios the mass concentrations and the differences between the curves increase, but there is no significant change in the overall shape.

The deviations between the results of the combined retrieval for $z_{N_0} = 1020$ m and the depolarization method are clearly larger. In the previous sections it was discussed that an underestimation of the particle amount in the near range would lead to an overestimation in higher atmospheric layers. Now the reverse case is shown. Especially the ash mass concentration is overestimated below 2 km with respect to the depolarization approach and therefore a significant deviation also appears between 2 and 3 km.

However, the second ash layer between 4 and 5 km is in better agreement with the depolarization method than in the previous calculations. The fine-mode fraction shows excellent agreement between 2 and 3 km, but between 0.5 and 2 km an underestimation with respect to the depolarization method occurs.

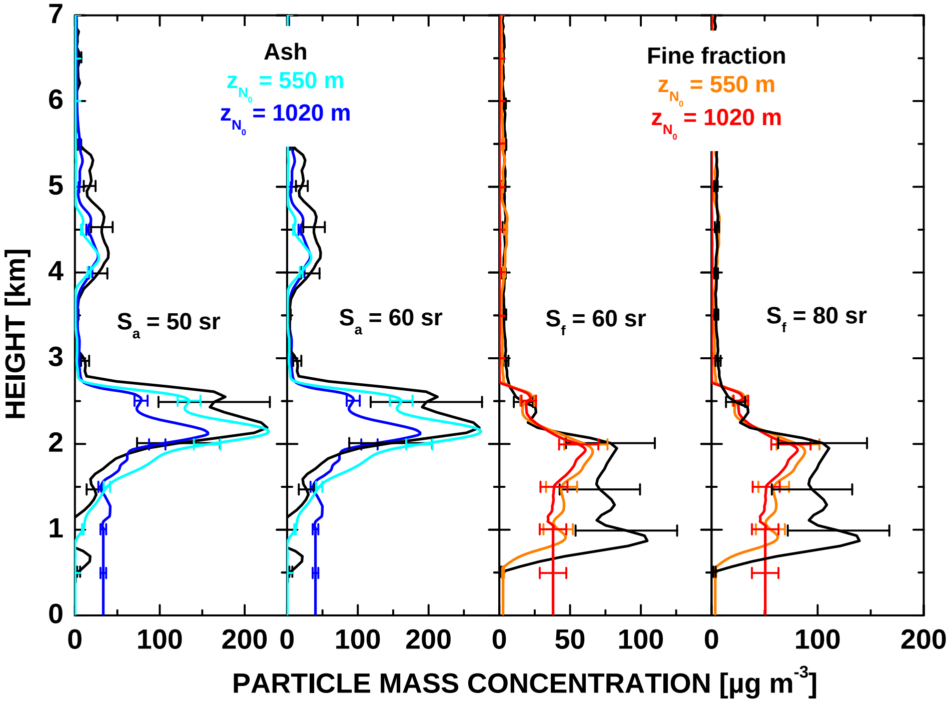

Figure 5.24: Mass concentrations for different lidar ratio assumptions of ash (red) and non-ash (blue) particles obtained from the combined retrieval algorithm for different z_{N_0}. They are calculated after Eq. (5.1) and (5.2). The black curves show the respective results obtained by the depolarization method (*Ansmann et al.*, 2011).

This case shows how important the additional use of near-range information is, which can be provided by a near-range telescope. While in the first calculation no contribution of volcanic ash is assumed for the lowermost 1000 m, the second case deals with constant concentrations in that range. Both assumptions can contain errors. By a comparison of the backscatter coefficients at 532 nm retrieved with the combined algorithm and with the Klett method (see Fig. 5.24) the difference can be explained. The depolarization approach is based on the backscatter profile derived with the Klett method. This profile shows considerably higher values in the range between 0.5 and 1.5 km than the recalculated profiles of the combined algorithm. Because no depolarization was obtained below 1.5 km, the difference is completely reflected in the fine-mode backscatter profiles.

In contrast, the ash backscatter profiles above 1.5 km are in very good agreement. The largest deviations occur for $z_{N_0} = 1020$ m which is caused by the overestimation in the near range.

Errors can occur, e.g., because the coarse mode is not necessarily caused only by ash particles. That would lead to an overestimation of the ash amount by the combined retrieval method. Also, the Klett method contains errors as already pointed out in the previous sections. That could explain the increasing deviations towards the ground. Especially for a mixed aerosol the lidar ratio is not constant as assumed using the Klett method. Further, the values used for the calculation of the mass concentration (see Eq. (5.1) and (5.2)) included uncertainties of 15% to 25%. Overlap effects can also not be ruled out even with correction. All in all, keeping these error sources in mind, one can conclude that the agreement is good regarding the classification of the aerosol types and the height of the aerosol layers as well as their extension. Especially the identification and quantification of ash via the depolarization ratio on the one hand and via the coarse-mode concentration on the other hand seems to work satisfactory and with similar error margins.

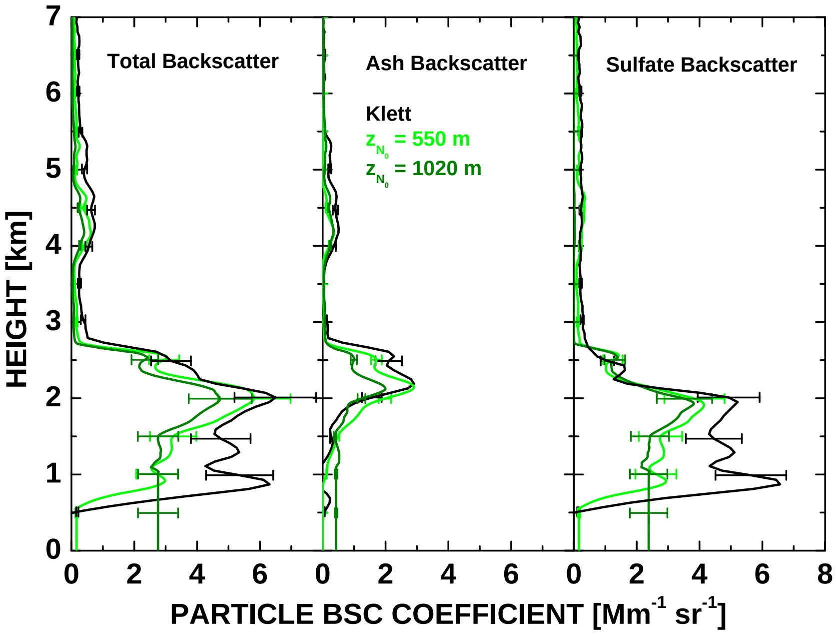

Figure 5.25: Comparison of the backscatter coefficients at 532 nm for $z_{N_0} = 550$ m (light green) and $z_{N_0} = 1020$ m (dark green) to the backscatter coefficient derived with the Klett method (black) between 14:01 UTC and 15:12 UTC on 19 April 2010.

Chapter 6

Conclusion and outlook

This work dealt with a numerical algorithm that was developed to obtain microphysical aerosol properties from combined lidar and sun photometer data. The retrieval of optical, microphysical, and radiative properties of aerosols from the single measurements is well established. To obtain more information about aerosol particles, the combination of both techniques is a promising approach. The underlying mathematical equations and physical processes, which are necessary to carry out such calculations, were described in detail.

The data which were used came from measurements with the Raman lidar MARTHA and a CIMEL sun photometer. Both instruments are installed at IfT Leipzig. In order to run the retrieval for the combination of both datasets, lidar and radiometric data have to be prepared. Raw lidar data were range- and overlap-corrected and afterwards the variation was calculated in order to quantify the error of the lidar measurements. Also, the reference point and the range of the profile could be determined. From sun photometer measurements the size distribution of the aerosol particles was obtained and further, by use of an inversion algorithm, corresponding values of backscatter and extinction coefficients were retrieved.

Finally, the retrieval algorithm delivered profiles of fine-mode and coarse-mode concentrations of the aerosol particles. Furthermore, backscatter and extinction coefficients for the three lidar wavelengths 355, 532, and 1064 nm as well as the lidar ratio at 532 nm were recalculated. This procedure was carried out for three cases which were characterized by different aerosol types. The case of 6 April 2009 was determined by East European aerosol that originated from combustion and industrial pollution. In May 2008 Saharan dust was transported to Leipzig and could be observed under clear-sky conditions, especially on 30 May 2008. The volcano eruption of the Eyjafjallajökull on 14 April 2010 provided a test case for the distinction of aerosol types. Beyond that, the cases were representative for a pure fine-mode event, a pure coarse-mode event, and a mixed aerosol.

The obtained backscatter and extinction profiles were used to compare the retrieval results with profiles determined with the Raman method and the Klett method. For the Saharan dust case good accordance for the range of the aerosol layer could be achieved. In case of the East European aerosol transport the backscatter profiles showed excellent agreement with only some deviations in the near range. Also, the particle mass concentrations obtained by the depolarization method (*Ansmann et al.*, 2011) in the ash cloud caused by the Eyjafjallajökull eruption could be confirmed. This leads to the conclusion that the retrieved concentration profiles of fine-mode and coarse-mode particles contain reliable information about the amount and type of aerosols in different height ranges. Lidar ratios could be used as an additional information to classify the aerosol.

The case of 19 April 2010 was chosen to carry out a distinction of aerosol types. Fine and coarse mode were assumed to be representative for sulfate and ash particles, respectively. In order to calculate particle mass concentrations, different backscatter coefficients for sulfate and ash were retrieved and compared to independent results published by *Ansmann et al.* (2011). While the calculation of the separated backscatter coefficients in *Ansmann et al.* (2011) is based on different depolarization ratios for ash and sulfate, the retrieval in this work is based on the separation of fine-mode and coarse-mode concentration profiles. Already in the total backscatter coefficient a difference was apparent in the range between 0.5 and 1.8 km. However, the obtained mass concentrations were in good agreement with only a difference in the non-ash mass concentration in the range between 0.5 and 2 km. Even though the error of the concentration profiles was found to be quite large, the discrepancies could not be explained completely. The reason is that not only the retrieval algorithm contains uncertainties, but also the Klett method and the parameters used for the calculation of the mass concentration can lead to erroneous results. Thus the differences in the total backscatter coefficient can be caused by both methods.

However, a qualitative statement about the aerosol type and concentration is possible, even though the quantitative result might have errors of the order of 50%. The identification of the aerosol layers, especially those with a large AOT, went quite well, so that the assignment of the radiometric data to vertically distributed aerosol layers can be done. It is one crucial problem of the sun photometer measurements that they do not contain information to which height range they refer. As radiometric measurements provide much more information than the one used in this work, a detailed classification of the aerosol would be possible in the future by continuing the work on combined retrieval algorithms.

The different concentration profiles which were obtained in dependence on z_{N_0} were also used for an error estimation. Mean profiles and the standard deviation were calculated and the uncertainty of the fine-mode and coarse-mode concentrations could be estimated. Large errors occur in the overlap-influence range and above the aerosol layer. Considering the individual cases and specifics, the relative error for the fine-mode concentration was found to be about 25% and for the coarse-mode concentration about 10%.

Problems which occur during lidar and sun photometer measurements show also up as critical issues in the combined retrieval algorithm. Lidar measurements are always affected by the overlap effect which can partly be corrected by use of overlap functions. For the influenced range in the low troposphere assumptions can be made, e.g., constant concentrations. Through varying heights z_{N_0} the influence of this assumption was investigated. In the case of 30 May 2008 significant differences occured only below z_{N_0}. For the case of 19 April 2010 a higher z_{N_0} resulted in an overestimation of the particle amount in the near range, whereas above z_{N_0} an underestimation occurred. It was shown that z_{N_0} has to be selected with care dependent on the individual characteristics of every measurement. The less the AOT is the more difficult is the retrieval of height profiles of optical and microphysical aerosol properties, especially if the aerosol is confined to the overlap-influenced range.

To further improve the retrieval algorithm for combined lidar and sun photometer data, first of all better daytime observations of lidar instruments are necessary. In addition, the installation of the near-range telescope at IfT, which is in use since September 2011, should provide datasets that are not significantly influenced by the overlap effect. Thus one of the reasons that lead to large uncertainties would be overcome. As not every lidar system is equipped with a near-range telescope, also an improvement in the algorithm itself is necessary. An approach which does not use constant profiles from the ground up to a certain hight could be prospective. If it were possible to adjust the concentration profiles in that range, the overestimation of aerosol content in higher atmospheric layers could be overcome. Further, it might be useful to constrain the algorithm in a way that above the aerosol layer fine-mode and coarse-mode concentrations are set to zero. The quicklooks provide a simple and fast tool to identify the upper limit of the aerosol layer. Lidar signals above that height usually contain only molecular background.

Another improvement would refer to the preparation of the radiometric data. For the Saharan dust case an unusual spectral behaviour of the backscatter coefficients occurred. The cause of this did not lie in the retrieval algorithm, but in the corresponding values of the backscatter coefficients retrieved from sun photometer measurements which are used as input data. Further studies have to be done to provide more information, so that better assumptions can be made. In particular, the assumed extinction-to-backscatter ratio and the parametrization of non-spherical particles lead to uncertainties. It would contribute to better results, if the problems that affect the input data can be overcome.

A new approach is the separation of the coarse mode into spherical and non-spherical particles while calculating backscatter and extinction coefficients from the radiometric measurements. This is currently implemented in the algorithm software. Other new features are the additional use of cross-polarized signals and the possibility to assimilate the parameters for the calculation of the molecular backscatter and extinction profiles. Furthermore, the retrieval algorithm itself is still under development. For instance, the optimization process will be based on the Levenberg–Marquardt method in the future. This method is known to lead to best results, even if the initial conditions are not optimal as it is the case for combined lidar and sun photometer measurements. Further studies will be done in order to quantify the influence of the algorithm parameters and thus to contribute to a field in aerosol research that becomes more and more important.

Bibliography

ACTRIS-Homepage (2011), ACTRIS – Aerosols, Clouds, and Trace gases Research InfraStructure Network, http://www.actris.net.

AERONET-Homepage (2011a), AERONET Aerosol Robotic Network, http://aeronet.gsfc.nasa.gov/new_web/index.html.

AERONET-Homepage (2011b), AERONET Inversion Products, *Tech. rep.*, NASA, http://aeronet.gsfc.nasa.gov/new_web/publications.html.

Ångström, A. (1929), On the atmospheric transmission of sun radiation and on dust in the air, *Geogr. Ann. Dtsch.*, *12*, 156–166.

Ansmann, A., and D. Müller (2005), Lidar and atmospheric aerosol particles, in *Lidar. Range-Resolved Optical Remote Sensing of the Atmosphere*, edited by C. Weitkamp, pp. 105–141, Springer, New York.

Ansmann, A., et al. (2010), The 16 April 2010 major volcanic ash plume over central Europe: EARLINET lidar and AERONET photometer observations at Leipzig and Munich, Germany, *Geophys. Res. Letts.*, *37*, L13810, doi:10.1029/2010GL043809.

Ansmann, A., et al. (2011), Ash and fine-mode particle mass profiles from EARLINET-AERONET observations over central Europe after the eruptions of the Eyjafjallajökull volcano in 2010, *J. Geophys. Res.*, *116*, D00U02, doi:10.1029/2010JD015567.

ARL-Homepage (2011), HYSPLIT – Hybrid Single Particle Lagrangian Integrated Trajectory Model, http://www.arl.noaa.gov/HYSPLIT_info.php.

Bösenberg, J., et al. (2003), EARLINET: A European Aerosol Research Lidar Network to establish an aerosol climatology, Report No. 348, *Tech. rep.*, Max Planck Institute for Meteorology, Hamburg, Germany, available at: *EARLINET-Homepage* (2011).

BSC-Homepage (2011), Homepage of the Barcelona Supercomputing Center: BSC-DREAM8b Model Info, http://www.bsc.es/plantillaH.php?cat_id=322.

Chaikovsky, A., O. Dubovik, P. Goloub, N. Balashevich, A. Lopatsin, Y. Karol, S. Denisov, and T. Lapyonok (2008), Software package for the retrieval of aerosol microphysical properties in the vertical column using combined lidar/photometer data (test version), *Tech. rep.*, Institute of Physics, National Academy of Sciences of Belarus, Minsk, Belarus, downloaded from http://dragon.bas-net.by/chaikovsky/LP-0_operational%20version%200/LP-0/Main/.

Dubovik, O. (2004), Optimization of numerical inversion photopolarimetric remote sensing, in *Photopolarimetry in Remote Sensing*, vol. 161, edited by G. Videen, Y. Yatskiv, and M. Mishchenko, pp. 65–106, Springer, doi:10.1007/1-4020-2368-5_3.

Dubovik, O., and M. D. King (2000), A flexible inversion algortihm for retrieval of aerosol optical properties from Sun and sky radiance measurements, *J. Geophys. Res.*, *105*, 20,673–20,696.

Dubovik, O., A. Smirnov, B. N. Holben, M. D. King, Y. J. Kaufman, T. F. Eck, and I. Slutsker (2000), Accuracy assessment of aerosol optical properties retrieval from AERONET sun and sky radiance measurements, *J. Geophys. Res.*, *105*, 9791–9806.

Dubovik, O., B. N. Holben, T. F. Eck, A. Smirnov, Y. J. Kaufman, M. D. King, D. Tanré, and I. Slutsker (2002a), Variability of absorption and optical properties of key aerosol types observed in worldwide locations, *J. Atmos. Sciences*, *59*, 590–608.

Dubovik, O., B. N. Holben, T. Lapyonok, A. Sinyuk, M. I. Mishchenko, P. Yang, and I. Slutsker (2002b), Non-spherical aerosol retrieval method employing light scattering by spheroids, *Geophys. Res. Letts.*, *10*, doi:10.1029/2001GL014506.

Dubovik, O., et al. (2006), Application of spheroid models to account for aerosol particle nonspericity in remote sensing of desert dust, *J. Geophys. Res.*, *11*, D11208, doi: 10.1029/2005JD006619.

Eadie, W. T. D., D. Drijard, F. E. James, M. Roos, and B. Sadoulet (1971), *Statistical Methods in Experimental Physics*, North-Holland Publishing Company, Amsterdam, London.

EARLINET-Homepage (2011), A European Aerosol Research Lidar Network to Establish an Aerosol Climatology: EARLINET, http://www.earlinet.org/index.php?id=earlinet_homepage.

Fernald, F. G. (1984), Analysis of atmospheric lidar observations: some comments, *Appl. Opt.*, *23*, 652–653.

FIRMS-Homepage (2011), Web fire mapper, http://firefly.geog.umd.edu:8080/firemap/.

Holben, B. N., et al. (1998), AERONET – A federated instrument network and data archive for aerosol characterization, *Remote Sens. Environ.*, *66*, 1–16.

King, M. D. (1982), Sensitivity of constrained linear inversions to the selection of the Lagrange multiplier, *J. Atmos. Sciences*, *39*, 1356–1369.

King, M. D., D. M. Byrne, B. M. Herman, and J. A. Reagan (1978), Aerosol size distributions obtained by inversion of spectral optical depth measurements, *J. Atmos. Sciences*, *21*, 2153–2167.

Klett, J. D. (1981), Stable analytic inversion solution for processing lidar returns, *Appl. Opt.*, *20*, 10,947–10,959.

Mattis, I., D. Müller, A. Ansmann, U. Wandinger, J. Preißler, P. Seifert, and M. Tesche (2008), Ten years of multiwavelength Raman lidar observation of free-tropospheric aerosol layers over Central Europe: Geometrical properties and annual cycle, *J. Geophys. Res.*, *113*, D20202, doi:10.1029/2007JD009636.

Müller, A. (2010), Mehrwellenlängen-Ramanlidar-Messungen über Leipzig von 2000–2010, Diploma Thesis, Universität Leipzig.

Müller, D., U. Wandinger, D. Althausen, I. Mattis, and A. Ansmann (1998), Retrieval of physical particle properties from lidar observations of extinction and backscatter at multiple wavelengths, *Appl. Opt.*, *37*, 2260–2263.

Müller, D., U. Wandinger, and A. Ansmann (1999a), Microphysical particle parameters from extinction and backscatter lidar data by inversion with regularization: Theory, *Appl. Opt.*, *38*, 2346–2357.

Müller, D., U. Wandinger, and A. Ansmann (1999b), Microphysical particle parameters from extinction and backscatter lidar data by inversion with regularization: Simulation, *Appl. Opt.*, *38*, 2358–2368.

Müller, D., I. Mattis, U. Wandinger, A. Ansmann, D. Althausen, and A.Stohl (2005), Raman lidar observations of aged Siberian and Canadian forest fire smoke in the free troposphere over Germany in 2003: Microphysical particle characterization, *J. Geophys. Res.*, *110*, D17201, doi:10.1029/2004JD005756.

Müller, D., A. Ansmann, I. Mattis, M. Tesche, U. Wandinger, D. Althausen, and G. Pisani (2007), Aerosol-type-dependent lidar ratios observed with Raman lidar, *J. Geophys. Res.*, *112*, D16202, doi:10.1029/2006JD008292.

Müller, D., et al. (2010a), Mineral dust observed with AERONET Sun photometer, Raman lidar and in situ instruments during SAMUM 2006: Shape-independent particle properties, *J. Geophys. Res.*, *115*, D07202, doi:10.1029/2009JD012520.

Müller, D., et al. (2010b), Mineral dust observed with AERONET Sun photometer, Raman lidar and in situ instruments during SAMUM 2006: Shape-dependent particle properties, *J. Geophys. Res.*, *115*, D11207, doi:10.1029/2009JD012523.

Nakajima, T., G. Tonna, R. Rao, P. Boi, Y. Kaufman, and B. Holben (1996), Use of sky brightness measurements from ground for remote sensing of particulate polydispersions, *Appl. Opt.*, *35*, 2672–2686.

Nickovic, S., G. Kallos, A. Papadopoulos, and O. Kakaliagou (2001), A model for prediciton of desert dust cycle in the atmosphere, *J. Geophys. Res.*, *106*, 18,113–18,129, doi:2000JD900794.

O'Neill, N. T., O. Dubovik, and T. F. Eck (2001), Modified Ångström exponent for the characterization of submicrometer aerosols, *Appl. Opt.*, *40*, 2368–2375.

O'Neill, N. T., T. F. Eck, A. Smirnov, B. N. Holben, and S. Thulasiraman (2003), Spectral discrimination of coarse and fine mode optical depth, *J. Geophys. Res.*, *108*, 4559, doi:10.1029/2002JD002975.

Pérez, C., S. Nickovic, J. M. Baldasano, M. Sicard, F. Rocadenbosch, and V. E. Cachorro (2006a), A long Saharan dust even over the western Mediterranean: Lidar, sun photometer observations, and regional dust modeling, *J. Geophys. Res.*, *111*, D15214, doi:10.1029/2005JD006579.

Pérez, C., S. Nickovic, G. Pejanovic, J. M. Baldasano, and E. Özsoy (2006b), Interactive dust-radiation modeling: A step to improve weather forecasts, *J. Geophys. Res.*, *111*, D16206, doi:10.1029/2005JD006717.

Press, W. H., S. A. Teukoisky, W. T. Vetterling, and B. P. Flannery (2007), *Numerical Recipes: The Art of Scientific Computing*, third ed., 1256 pp., Cambridge University Press.

Reagan, J. A., J. D. Spinhirne, and D. M. Byrne (1977), Atmospheric Particulate Properties Inferred from Lidar and Solar Radiometer Observations Compared with Simultaneous *In Situ* Aircraft Measurements: A Case Study, *J. Appl. Meteor.*, *16*, 911–928.

Sinyuk, A., et al. (2007), Simultaneous retrieval of aerosol and surface properties from a combination of AERONET and satellite data, *Remote Sens. Environ.*, *107*, 90–108.

Smirnov, A., B. N. Holben, T. F. Eck, O. Dubovik, and I. Slutsker (2000), Cloud-screening and quality control algorithms for the AERONET database, *Remote Sens. Environ.*, *73*, 337–349.

Spinhirne, J. D., J. A. Reagan, and B. M. Herman (1980), Vertical distribution of aerosol extinction cross section and inference of aerosol imaginary index in the troposphere by lidar technique, *J. Appl. Meteor.*, *19*, 426–438.

Stohl, A., and D. J. Thomson (1999), A density correction for Lagrangian particle dispersion models, *Boundary-Layer Meteorol.*, *90*, 155–167.

Stohl, A., M. Hittenberger, and G. Wotawa (1998), Validation of the Lagrangian particle dispersion model FLEXPART against large scale tracer experiment data, *Atmos. Env.*, *32*, 4245–4264.

Stohl, A., C. Forster, A. Frank, P. Seibert, and G. Wotawa (2005), Technical note: The Lagrangian particle dispersion model FLEXPART version 6.2, *Atmos. Chem. Phys.*, *5*, 2461–2474.

Tesche, M., A. Ansmann, D. Müller, D. Althausen, R. Engelmann, V. Freudenthaler, and S. Groß (2009a), Separation of dust and smoke profiles over Cape Verde by using multiwavelength Raman and polarization lidars during SAMUM 2008, *J. Geophys. Res.*, *114*, D13202, doi:10.1029/2009JD011862.

Tesche, M., et al. (2009b), Vertical profiling of Saharan dust with Raman lidars and airborne HSRL in southern Morocco during SAMUM, *Tellus, Ser. B*, *61*, 144–164.

Tikhonov, A. N., and V. Y. Arsenin (1977), *Solution of ill-posed problems*, 258 pp., Winston.

Twomey, S. (1977), *Introduction to the Mathematics of Inversion in Remotes Sensing and Indirect Measurements*, Elsevier Scientific, New York.

Wandinger, U. (2005), Introduction to lidar, in *Lidar. Range-Resolved Optical Remote Sensing of the Atmosphere*, edited by C. Weitkamp, pp. 1–16, Springer, New York.

Wandinger, U., and A. Ansmann (2002), Experimental determination of the lidar overlap profile with Raman lidar, *Appl. Opt.*, *41*, 511–514.

Wandinger, U., A. Hiebsch, I. Mattis, G. Pappalardo, L. Mona, and F. Madonna (2010), Aerosols and clouds: Longterm database from spaceborne lidar measurements, *Tech. rep.*, Leipzig, Germany and Potenza, Italy, ESTEC Contract 21487/08/NL/HE, Final Report.

Wandinger, U., et al. (2002), Optical and microphysical characterization of biomass-burning and industrial-pollution aerosols from multiwavelength lidar and aircraft measurements, *J. Geophys. Res.*, *107*, 8125, doi:10.1029/2000JD000202.

Wandinger, U., et al. (2004), Air mass modification over Europe: EARLINET aerosol observations from Wales to Belarus, *J. Geophys. Res.*, *109*, D24205, doi:10.1029/2004JD005142.

List of Figures

List of Tables

Acknowledgment

I wish to thank Dr. habil. Albert Ansmann and Prof. Dr. Manfred Wendisch for reviewing this master thesis and for enabling me to work on this topic. A special thanks is addressed to Dr. Ulla Wandinger for the excellent supervision and the careful proofreading.

I wish to thank all members of the lidar group for their friendly inclusion and cooperation. They never hesitated to answer my questions and to provide data, particularly Dr. Ronny Engelmann, Anja Hiebsch, Jörg Schmidt, and Dr. Patric Seifert.

I would like to thank Anatoli Chaikovsky and his work group at the Institute of Physics in Minsk for the supply of the software on which this work is based. Beyond that they helped with technical and scientific advice.

Last, but not least, I thank my boyfriend Martin Treffkorn for supporting me and the constructive discussions. I also like to thank Friederike Höpner for the amusing lunch and coffee breaks which were good distractions from work.